International Journal of Multiphase Flow 184 (2025) 105111

Contents lists available at ScienceDirect

International Journal of Multiphase Flow

journal homepage: www.elsevier.com/locate/ijmulflow

Research Paper

Correlations for aerodynamic force coefficients of non-spherical particles in compressible flows

Christian Gorges [a], Victor Chéron [a], Anjali Chopra [a], Fabian Denner [b], Berend van Wachem [a,*]

[a] Chair of Mechanical Process Engineering, Otto-von-Guericke-Universität Magdeburg, Universitätsplatz 2, 39106 Magdeburg, Germany
[b] Department of Mechanical Engineering, Polytechnique Montréal, Montréal, H3T 1J4, QC, Canada

ARTICLE INFO

Dataset link: 10.5281/zenodo.14283844

Keywords:
Compressible flow
Non-spherical particles
Drag
Lift
Torque

ABSTRACT

This study presents particle-resolved direct numerical simulations using three-dimensional body-fitted hexahedral meshes to investigate the aerodynamic force and torque coefficients of non-spherical particles in compressible flows. The simulations focus on three particle shapes: a prolate spheroid, an oblate spheroid, and a rod-like particle, across a range of Mach numbers (0.3 to 2.0), angles of attack (0° to 90°), and particle Reynolds numbers (100 to 300). Results show that the particle shape significantly impacts the aerodynamic forces on a particle in a compressible flow, with oblate spheroids exhibiting the highest drag, lift, and torque values. Correlations for these aerodynamic coefficients of the particles in a compressible flow are developed and validated. These correlations advance multiphase flow modelling by improving the accuracy of point-particle simulations for non-spherical particles in compressible flows.

1. Introduction

Particle-laden flows are of significant scientific interest due to their ubiquity and application in many industrial processes. In nature, examples of particle-laden flows are dust storms, volcanic eruptions, sediments in water bodies, eroding soils, the dispersion of aerosols, and blood flow. They are also applied in many modern technologies in industries such as aerospace, medicine and engineering. Some examples are solid-propellant rocket combustion (Carlson and Hoglund, 1964), transdermal injections (Hogan et al., 2015), inhalers (Capecelatro et al., 2022), and spray coating (Villafuerte, 2015). Such flows involve complex particle–fluid and particle–particle interactions at varying time and length scales, which makes it essential to understand the flow physics in order to design systems that are efficient and cost-effective.

Particle-resolved direct numerical simulations (PR-DNS) of particle-laden flows require tremendous computational resources. However, a point-particle approach can significantly reduce the computational power required to model particle-laden flows. This approach requires force models to determine the forces exerted on the particles by the surrounding fluid, as well as by contact with other particles (Michaelides et al., 2022). In this context, several force models have been developed which are applicable for various flow regimes and volume fractions (Tenneti et al., 2011; Zastawny et al., 2012; Loth, 2008; Loth et al., 2021; Sanjeevi et al., 2018, 2022; Clift and Gauvin, 1971; Henderson, 1976; Parmar et al., 2010; Chéron et al., 2024). In order to derive these correlations, it is essential to first understand the behaviour of an isolated particle and the forces experienced by the particle in various flow regimes. These force correlations can then be extended to multi-particle systems.

Forces acting on an isolated particle depend on several factors, such as the particle Reynolds number, the Mach number, the fluid properties, the particle shape, and angle of attack between the mean fluid flow and the axis of the particle. Predicting the forces that act on a particle in a fluid flow and predicting its behaviour have been the subject of studies for decades (Stokes, 1851; Wadell, 1934; Henderson, 1976; Rosendahl, 2000; Hölzer and Sommerfeld, 2008; Mando and Rosendahl, 2010; Tenneti et al., 2011; Nagata et al., 2016, 2018, 2020a; van Wachem et al., 2015). One of the first analytical models to predict the drag of a spherical particle for particle Reynolds numbers in the Stokes regime ($\mathrm{Re}_p \ll 1$) was given by Stokes (1851) as $C_D = 24/\mathrm{Re}_p$ where C_D is the drag coefficient. This model is the basis for later proposed drag models (Kaskas, 1964; Carlson and Hoglund, 1964; Happel and Brenner, 1981; Salman and Verba, 1988), applicable to various flow regimes and practical applications.

Since particles are not limited to spherical shapes, the proposed models also included non-spherical particle shapes. Some of the most notable correlations for non-spherical particle shapes were those presented by Zastawny et al. (2012), Ouchene et al. (2015, 2016), Sanjeevi

* Corresponding author.
E-mail address: berend.vanwachem@multiflow.org (B. van Wachem).

https://doi.org/10.1016/j.ijmultiphaseflow.2024.105111
Received 26 August 2024; Received in revised form 9 December 2024; Accepted 16 December 2024
Available online 20 December 2024
0301-9322/© 2024 The Authors. Published by Elsevier Ltd. This is an open access article under the CC BY-NC-ND license (http://creativecommons.org/licenses/by-nc-nd/4.0/).

et al. (2018, 2022), and Chéron et al. (2024), Chéron and van Wachem (2024). Zastawny et al. (2012) proposed shape-specific correlations for prolate and oblate spheroids, as well as rod-like particles using PR-DNS. They are the most widely used correlations for non-spherical particles in incompressible flows. A detailed analysis of various correlations for prolate spheroids has been performed by Ouchene et al. (2015). They conclude that, while the correlation of Zastawny et al. (2012) predict the aerodynamic coefficients for the ellipsoidal particles accurately, the correlations of Zastawny et al. (2012) only consider ellipsoidal particles with two different aspect ratios. To address this, Ouchene et al. (2016) propose new correlations for drag, lift and torque, which are valid for aspect ratios ranging from $1-32$ of prolate particles. Another recent study on non-spherical particles has been conducted by Sanjeevi et al. (2018) using the Lattice-Boltzmann method. The shape-specific correlations proposed by them are applicable for particle Reynolds numbers $\mathrm{Re_p}$ ranging from the Stokes limit to 2000, and depend on the particle Reynolds number and the angle of attack of the particle. They extended the correlation to include prolate particles with different aspect ratios, the upper limit of the aspect ratio being 32 (Sanjeevi et al., 2022). More recently, shape-dependent correlations have been extended to accurate correlations to predict the interaction forces between non-spherical particles and locally uniform and non-uniform fluid flow, including the aspect ratio (Fröhlich et al., 2020; Ouchene, 2020; Sanjeevi et al., 2022; Chéron et al., 2024).

Drag predictions for non-spherical particles in the incompressible regime have received significant attention in recent years, and the proposed correlations are becoming more and more accurate by considering locally non-uniform fluid flow due to shear effects (Dabade et al., 2016; Chéron et al., 2024) and wall effects (Fillingham et al., 2021; Bhagat and Goswami, 2022; Chéron and van Wachem, 2024). However, correlations for compressible particle-laden flows have not seen much development, as the prediction of aerodynamic coefficients is much more complex in this case (Capecelatro and Wagner, 2024). In compressible flows, the particle behaviour depends not only on the particle Reynolds number, the particle shape, and the angle of attack, but also on the Mach number of the flow relative to the particle. The forces experienced by the particles are affected by high-speed flow phenomena, such as the formation of shock waves, and their interaction with the particle (Capecelatro and Wagner, 2024). Moreover, non-continuum effects due to rarefaction of the gas must also be considered, which occur when the mean free path of the gas molecules is comparable to the characteristic length of the particle. This requires a deeper understanding of the flow physics around the particle in a compressible regime.

Bashforth (1870) describes experiments with cannonballs, and shows the effect of compressibility on the drag force in the subsonic, transonic and supersonic regimes ($0.3 \leq \mathrm{Ma} \leq 2.0$). In this study, they found the drag force to be proportional to the square of the velocity in the subsonic and supersonic regimes and, proportional to the cube of velocity in the transonic regime. This is an important observation in regard to the effect of compressibility on the drag force. Later, Carlson and Hoglund (1964) propose a drag correlation for spherical particles in a compressible flow, also including rarefaction effects. This model is applicable for $\mathrm{Ma} \leq 2$ and $10^{-1} \leq \mathrm{Re_p} \leq 10^3$. Subsequently, Henderson (1976) also propose a Reynolds number and Mach number dependent correlation for spherical particles, valid for a larger range of $\mathrm{Re_p} \leq 2 \times 10^4$ and $\mathrm{Ma} \leq 6$ based on existing experimental data. Loth (2008) show that $\mathrm{Re_p} \approx 45$ separates the compression-dominated ($\mathrm{Re_p} \gtrapprox 45$) and rarefaction-dominated ($\mathrm{Re_p} \lessapprox 45$) regimes.

Another noteworthy study on the effects of compressibility for an isolated spherical particle is presented in Nagata et al. (2016). They perform an extensive PR-DNS study to quantify drag, lift and torque for Reynolds numbers in the range of $50-300$ and Mach numbers in the range of $0.3-2.0$. They show that increasing the Mach number leads to an increase of the drag coefficient due to the formation of a detached shock wave in the supersonic regime. A comparison of the drag coefficients obtained using PR-DNS with the existing drag correlations (Carlson and Hoglund, 1964; Clift and Gauvin, 1971; Henderson, 1976) reveal that there exists a significant variation among the correlations in transonic and supersonic regimes. In order to investigate the effect of the Mach number and the particle Reynolds number on the flow field, Nagata et al. (2020a) present an experimental study using Schlieren images for $10^3 \leq \mathrm{Re_p} \leq 10^5$ and $0.9 \leq \mathrm{Ma} \leq 1.6$. They found that the oscillations of the wake and its size decrease with decreasing $\mathrm{Re_p}$ for the considered range of Reynolds numbers. This behaviour is opposite to the one observed for $\mathrm{Re_p} \leq 10^3$. Moreover, the wake structure amplitude decreases with increasing Mach numbers. Using PR-DNS, Nagata et al. (2020b) examines the change in drag coefficient due to changing $\mathrm{Re_p}$ and Ma based on the location of the separation point on the sphere.

Subsequently, Loth et al. (2021) propose a drag model for spherical particles derived by combining existing experimental and numerical data from various sources (Loth, 2008; Parmar et al., 2010; Jacobs, 1929; Roos and Willmarth, 1971; Short, 1967; Spearman and Braswell, 1993; Theofanous et al., 2018; Nagata et al., 2016, 2020b). This model encompasses a wide range of Reynolds and Mach numbers to take into account the continuum- and rarefaction-dominated regimes, with a focus on the quasi-nexus at $\mathrm{Re_p} \approx 45$. The model seems to be the most accurate drag model developed so far that predicts drag of a sphere in a compressible flow in various regimes, including the quasi-nexus that occurs when the flow transitions from the rarefaction-dominated to the compression-dominated regime. All available drag models have recently been summarized and reviewed in detail by Capecelatro (2022), including theoretical and experimental work in the field of gas–solid flows with spherical particles. They discuss the challenges that lie in the realm of modelling compressible flows, such as additional time and length scales due to the presence of shock waves. The comprehensive review sheds light on the unavailability of drag correlations for multi-particle systems in compressible flows. They suggest using a modified Loth model for isolated particles, which incorporates the volume fraction as presented in Tenneti et al. (2011). A more recent development with respect to the drag model for compressible flows is presented in Singh et al. (2022), which aims to make existing drag correlations for spherical particles more accurate. The proposed drag model takes into account the surface temperature, the specific heat ratio, and other thermodynamic parameters to incorporate the effects of the gas surrounding the particle. Moreover, their model is applicable for all flow regimes classified according to the Knudsen number, that is, from the continuum regime with $\mathrm{Kn} < 0.01$ to the rarefied regime with $\mathrm{Kn} > 10$, including intermediate slip and transitional flow regimes ($0.01 < \mathrm{Kn} < 10$).

Research to date on the forces on particles in compressible flows has only considered perfectly spherical particles, and the effect of the particle shape on the aerodynamic coefficients has not yet been investigated. The available correlations, therefore, miss important aspects of the flow physics for non-spherical particles. For example, no transverse force acts on spherical particles, which is not the case for non-spherical particles. Such correlations for lift, drag and torque prediction using such an assumption cannot be used to represent an array of various particle shapes that exist in practical applications.

In this study, we address this gap by conducting PR-DNS of three shapes of non-spherical particles in compressible flows, in the range $100 \leq \mathrm{Re_p} \leq 300$ and $0.3 \leq \mathrm{Ma} \leq 2$. The particle shapes and their aspect ratios ($\beta = a/b$) considered in the current study are: a prolate spheroid ($\beta = 5/2$), an oblate spheroid ($\beta = 5$), and a rod-like particle ($\beta = 5$). We have also carried out simulations with spherical particles for validation purposes. Based on our PR-DNS results, we derive correlations to predict the lift, drag and torque for non-spherical particles in compressible flows, considering the Mach number, the particle Reynolds number, the particle shape, and the angle of attack. The current study focuses on the compression-dominated flow regime, which corresponds to $\mathrm{Re_p} > 50$ and $\mathrm{Kn} < 0.01$.

2. Methodology

PR-DNS are performed with a 3-dimensional body-fitted mesh for the various particle shapes using a finite-volume based in-house compressible flow solver. The fully-coupled pressure-based algorithm described in Xiao et al. (2017) and Denner et al. (2020) is used to solve the equations governing a compressible flow as follows:

$$\frac{\partial \rho}{\partial t} + \frac{\partial(\rho u_i)}{\partial x_i} = 0, \tag{1}$$

$$\frac{\partial(\rho u_i)}{\partial t} + \frac{\partial(\rho u_i u_j)}{\partial x_j} = -\frac{\partial p}{\partial x_i} + \frac{\partial \tau_{ij}}{\partial x_j}, \tag{2}$$

$$\frac{\partial(\rho h)}{\partial t} + \frac{\partial(\rho h u_i)}{\partial x_i} = \frac{\partial p}{\partial t} - \frac{\partial q_i}{\partial x_i} + \frac{\partial(\tau_{ij} u_j)}{\partial x_i}, \tag{3}$$

where ρ is the density, $\mathbf{u}$ is the fluid velocity, p is the pressure, $\boldsymbol{\tau}$ is the shear stress tensor, h is the specific total enthalpy, and $\mathbf{q}$ is the conductive heat flux. This set of equations is closed by the ideal gas equation of state, and the constitutive equation for a Newtonian fluid,

$$\tau_{ij} = -p\delta_{ij} + \mu\left[\frac{\partial u_i}{\partial x_j} + \frac{\partial u_j}{\partial x_i}\right] - \frac{2}{3}\mu\frac{\partial u_k}{\partial x_k}\delta_{ij} \tag{4}$$

where μ is the fluid viscosity. The reference temperature is set to $\theta_0 = 300$ K and the reference pressure to $p_0 = 1.0\times10^5$ Pa. Based on the properties of air, the ratio of specific heats is $\gamma = 1.4$ and the specific heat capacity at constant pressure is $c_p = 1008$ J/(kg K). The thermal conductivity and viscosity of the fluid are calculated for various Ma and $\mathrm{Re_p}$ such that the Prandtl number, Pr, of the gas is maintained at 0.71. Furthermore, the viscosity is assumed to be constant in the domain. The free stream density is set to $\rho_\infty = 1.1574$ kg/m^3, whereas the free stream fluid velocity is determined based on the prescribed Ma and $\mathrm{Re_p}$ for each simulation.

Both the transient and the spatial terms are discretized using second-order accurate schemes. The second-order accurate backward Euler scheme is used for the temporal discretization and the TVD Minmod scheme is used for spatial discretization within the finite-volume framework. The fully-coupled pressure-based algorithm ensures a strong pressure–velocity and pressure–density coupling, and allows simulating a wide range of Mach numbers and does not require an under-relaxation parameter to ensure convergence (Xiao et al., 2017; Denner et al., 2020).

The fluid flow over a fixed, isolated particle is simulated in a spherical domain with radius R, where the particle lies at the centre of the domain. A spherical domain is chosen because the orientation of the particle relative to the flow can be changed without having to reconstruct the mesh. The desired angle of attack, α, which is the angle between the inflow velocity vector and the chord line of the particle, is obtained by rotating the domain boundaries. The hemispherical caps of the domain are set to be the inlet and outlet boundaries, as illustrated in Fig. 1. For compressible flows, the inlet hemisphere is prescribed with Dirichlet boundary conditions for velocity, pressure, and temperature, whereas the outlet hemisphere is prescribed with Neumann boundary conditions. The particle boundary is simulated as a no-slip wall with an adiabatic boundary condition for temperature. The computational domain is discretized using a hexahedral non-uniform body-conforming mesh, with smaller cells near the particle and increasingly larger cells towards the domain boundary. The radius of the domain is $R = 50c$, where c is the semi-major axis of the particle. The particle shapes and their aspect ratios ($\beta = a/b$) considered in the current study are: a prolate spheroid ($\beta = 5/2$), an oblate spheroid ($\beta = 5$), and a rod-like particle ($\beta = 5$). The discretized domains for the considered particle shapes are shown in Fig. 2.

In Appendix A, Figs. A.15 to A.17 show convergence studies for the three considered non-spherical particle shapes for a Reynolds number of 300, Mach numbers of 0.3 and 2, and an angle of attack of 0°. Based on the results of the convergence studies in Appendix A, the medium-sized mesh is chosen for all simulations of all three non-spherical shapes

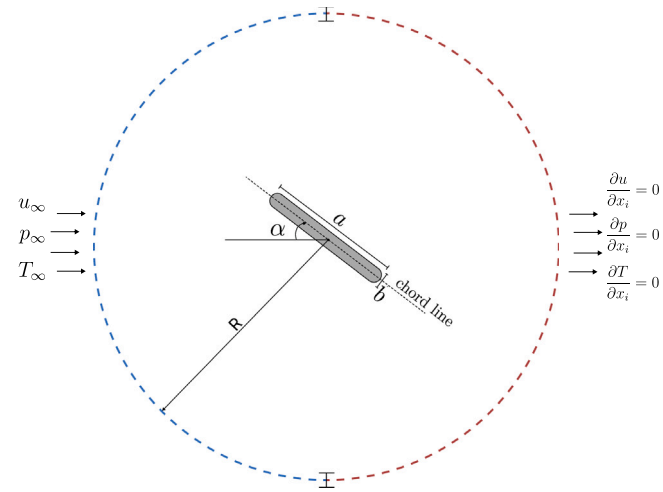

Fig. 1. An illustration of the domain and the boundary conditions for the simulations in the current study. The particle is fixed at the centre of the spherical domain with hemispherical caps as the inlet (blue) and outlet (red) boundaries. The angle of attack of the particle is changed by rotating the hemispherical caps. It should be noted that the illustration is not to scale, as $R \gg \{a, b\}$. (For interpretation of the references to colour in this figure legend, the reader is referred to the web version of this article.)

as it gives the best trade-off between accuracy and computational cost. Compared to the fine mesh, the relative error of the drag coefficient for the medium is below 5% for all convergence studies, except for the prolate spheroid at Ma = 2 where the error is 6%. The ratio of the equivalent diameter of a sphere of the same volume to the smallest mesh spacing at the particle surface is 75 ($\Delta x = 0.072$ m) for the prolate spheroid, 115 ($\Delta x = 0.051$ m) for the oblate spheroid and 50 ($\Delta x = 0.0019$ m) for the rod-like particle, which leads to a resolved boundary layer for all 3 non-spherical particle shapes.

The force $\mathbf{F}$ and the torque $\mathbf{T}$ acting on the surface of the particles are computed by

$$F_i = \int_S \tau_{ij} n_j \,\mathrm{d}S, \tag{5}$$

$$T_i = \int_S \epsilon_{ijk} r_j \tau_{km} n_m \,\mathrm{d}S, \tag{6}$$

where S is the surface of the particle, $\mathbf{n}$ is the normal vector to the particle surface, $\mathbf{r}$ is the vector from the particle centre to the point where the force is applied on the particle surface, and ϵ is Levi-Civita symbol for the cross product. The corresponding coefficients are defined as

$$C_\mathrm{D} = \frac{F_\mathrm{D}}{\frac{1}{2}\rho_\infty u_\infty^2 A_\mathrm{p}},\ C_\mathrm{L} = \frac{F_\mathrm{L}}{\frac{1}{2}\rho_\infty u_\infty^2 A_\mathrm{p}},\ C_\mathrm{M} = \frac{T_\mathrm{p}}{\frac{1}{2}\rho_\infty u_\infty^2 \pi d_\mathrm{p}^3/8}, \tag{7}$$

where F_D and F_L are the forces acting parallel and normal to the flow direction, respectively, T_p is the pitching torque acting on the particle, ρ_∞ is the free stream density, u_∞ is the free stream velocity, and $A_\mathrm{p} = \pi d_\mathrm{p}^2/4$ is the reference area of the particle based on the equivalent diameter of a sphere of the same volume, d_p.

The time step is constrained by setting the maximum Courant–Friedrichs–Lewy (CFL) number to 0.3. The simulations are run until a steady state is observed in the temporal evolution of the aerodynamic force coefficients. The residuals have a convergence criterion of $O(10^{-8})$ and a total conservation error of $O(10^{-3})$ is achieved. All aerodynamic force coefficients shown in the results section are mean values of at least the last 1000 time steps.

3. Results and discussion

In this section, the PR-DNS results are first validated with results for particles in incompressible and compressible flows reported in the

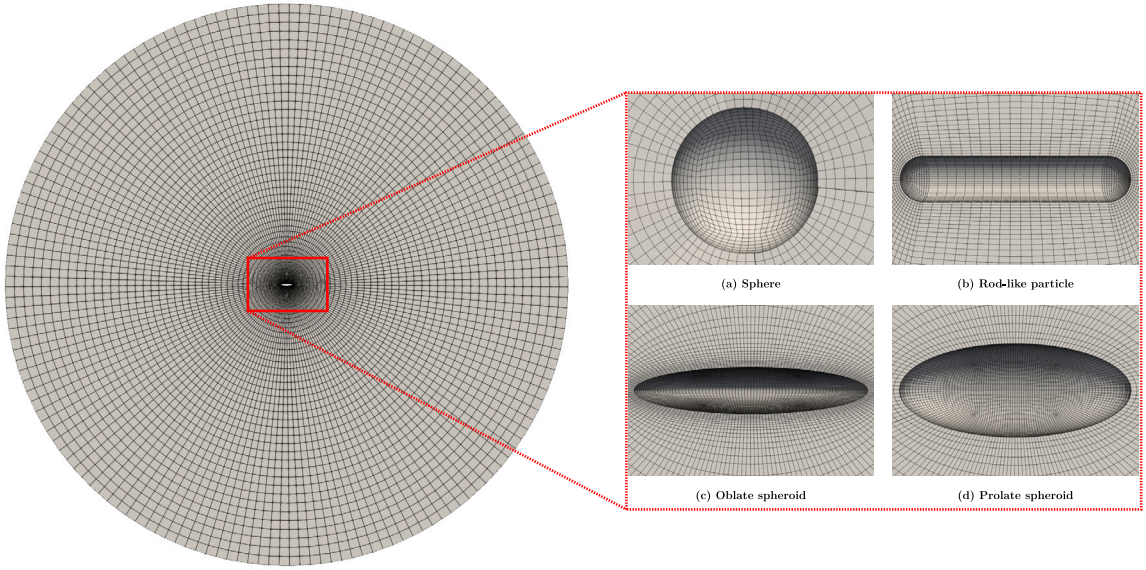

Fig. 2. A slice of the body-fitted hexahedral base mesh for the particle shapes used in the current study.

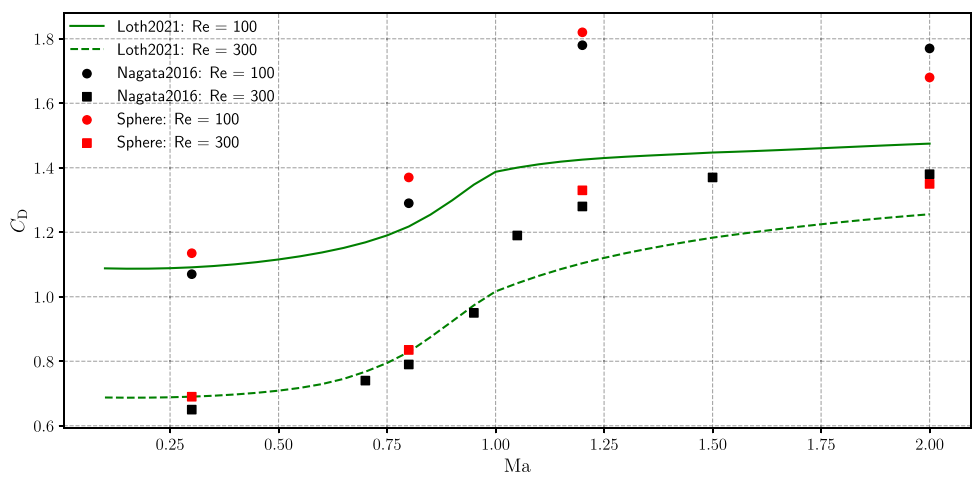

Fig. 3. The drag coefficient as a function of the Mach number for an isolated sphere in a compressible flow for particle Reynolds numbers of 100 and 300, compared against the PR-DNS data from Nagata et al. (2016) and the correlation of Loth et al. (2021).

literature. Subsequently, the flow regimes and the aerodynamic force coefficients obtained for the considered non-spherical particles are presented and discussed.

3.1. Validation

The methodology in the current study is validated with the available data in the literature for a spherical particle in various flow regimes (from the incompressible limit at Ma = 0.3 to supersonic flow at Ma = 2), and non-spherical particles in the incompressible limit.

The drag experienced by an isolated spherical particle for particle Reynolds numbers of 100 and 300 is compared with the PR-DNS data of Nagata et al. (2016) and the compressible drag model of Loth et al. (2021) as shown in Fig. 3. For all Mach numbers, results from the current simulations show good agreement with the PR-DNS data of Nagata et al. (2016) and reasonable agreement with the model of Loth et al. (2021), while the drag coefficient for supersonic Mach numbers predicted by our simulations agree better with the data of Nagata et al. (2016). It is, however, important to note that the transonic regime is not very well documented in the literature and that the existing data shows a lot of variation. Overall, the results for the sphere in compressible flow obtained in this work agree well with the existing literature.

Fig. 4 shows a comparison of the simulation results for the prolate spheroid in the incompressible limit (Ma = 0.3) for a particle Reynolds number of 300 with the correlations of Sanjeevi et al. (2018) and Zastawny et al. (2012) for a prolate spheroid in incompressible flow. Furthermore, Fig. 5 shows a comparison of the simulation results for the rod-like particle in the incompressible limit (Ma = 0.3) for a Reynolds number of 300 with the data of Chéron et al. (2024) for the same rod-like particle in incompressible flow. The results obtained for the rod-like particle match very well with the data of Chéron et al. (2024). The results obtained for the prolate spheroid match the correlations of Zastawny et al. (2012) and Sanjeevi et al. (2018) very well.

Fig. 6 shows the local Mach number and the local Knudsen number for the oblate spheroid at $\mathrm{Re_p} = 300$ and $\alpha = 45°$. The oblate spheroid in this flow configuration is one of the most extreme flow conditions in this work. As visible from Fig. 6, the local Mach number reaches a maximum of 2.2 and the local particle Knudsen number, computed as (Loth et al., 2021)

$$\mathrm{Kn_{local}} = \sqrt{\frac{\pi\gamma}{2}}\left(\frac{\mathrm{Ma_{local}}}{\mathrm{Re_{local}}}\right) \tag{8}$$

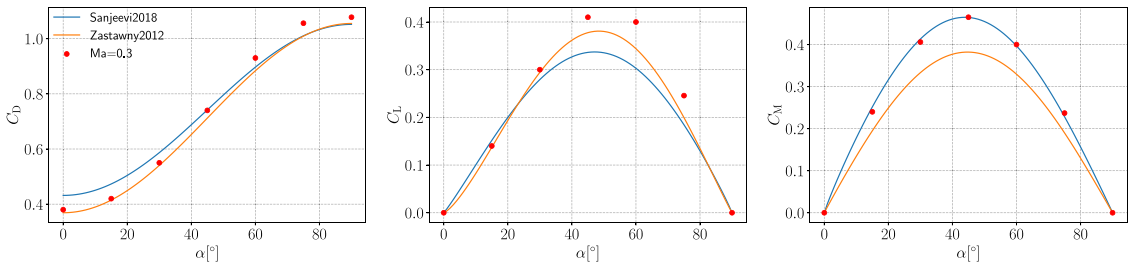

Fig. 4. Comparison of our data with the correlations of Sanjeevi et al. (2018) and Zastawny et al. (2012) for the prolate spheroid in an incompressible flow at the incompressible limit of Ma = 0.3 at a particle Reynolds number of 300 for all three aerodynamic force coefficients.

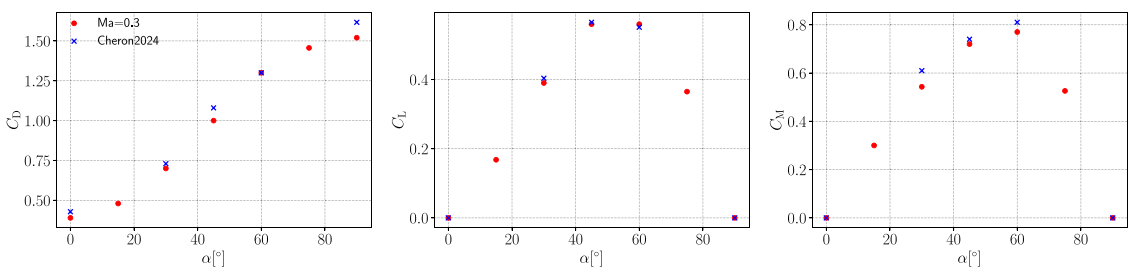

Fig. 5. Comparison of our data with the correlations of Chéron et al. (2024) for the rod-like particle in incompressible flow to the incompressible limit simulations of Ma = 0.3 at a particle Reynolds number of 300 for all three aerodynamic force coefficients.

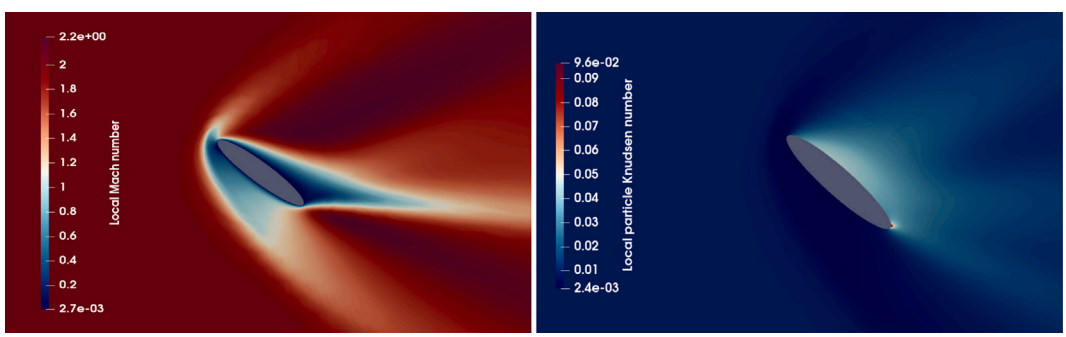

Fig. 6. Contour plots of the local Mach number (left) and of the local particle Knudsen number (right) for the oblate spheroid at $Re_p = 300$ and $\alpha = 45°$.

reaches a maximum of 0.096 at the lower tip of the particle surface. Although a part of the flow in the wake of the particle is in the slip regime ($0.01 < Kn < 0.1$), the flow is still dominated by the continuum regime ($Kn \ll 0.1$). The continuum assumption, thus, forms an adequate basis for the conducted simulations.

3.2. Non-spherical particles in compressible flow

In this section, the results obtained from the PR-DNS with non-spherical particles in a compressible flow are shown. First, some representative contour plots of the velocity field are shown, which are analysed for the different particle shapes and configurations, and compared with each other. Subsequently, the results for the aerodynamic force coefficients are presented and discussed.

Figs. 7–9 show the steady-state velocity flow fields for all three non-spherical particle shapes for a Reynolds number of 300 and Mach numbers of 0.8 and 2, for angles of attack of 0°, 45°, and 90°. These two Mach numbers are representative examples of the flow fields in the transonic (Ma = 0.8) and supersonic (Ma = 2) regimes. The flow fields of the other Mach numbers do not differ significantly from the two shown. The same applies to the Reynolds number. The flow fields at a Reynolds number of 100 differ for the most part only in magnitude compared to a Reynolds number of 300.

When comparing the velocity fields for Ma = 2, as shown in Figs. 7–9 it becomes clear that the oblate spheroid shape forms the largest bow shock in front of the particle, followed by the rod-like particle, and the prolate spheroid with the smallest bow shock for all three angles. This observation goes hand in hand with the aspect ratios or sphericity of the respective particles. The prolate spheroid shape has the lowest aspect ratio and the fewest "sharp" edges or regions of high curvature, whereas the oblate spheroid shape has the most obvious "sharp" edges.

Considering the transonic regime (Ma = 0.8) for all three particle shapes, one can observe that the oblate spheroid is the only shape where the velocity field shows an unsteady and oscillating behaviour in the wake behind the particle for angles of attack of 45° and 90°. This behaviour is not observed for the other two shapes and also not for the simulations of the oblate spheroid with Reynolds number 100. Furthermore, for all three shapes the bow shock in front of the particles starts to form but, is not fully formed in the transonic regime. Comparison of the transonic regime with the supersonic regime also shows that the wake behind the particles is longer in the transonic regime and shorter in the supersonic regime.

Fig. 10 presents the drag coefficients, C_D, for all three non-spherical particle shapes as a function of the Mach number for all considered angles of attack. The lift and torque coefficients as a function of the Mach number for all three non-spherical particle shapes are shown in Appendix B.

For a given Mach number, the magnitudes of the drag coefficients for all three non-spherical particle shapes in Fig. 10 increase with increasing angle of attack. Furthermore, as already indicated by the

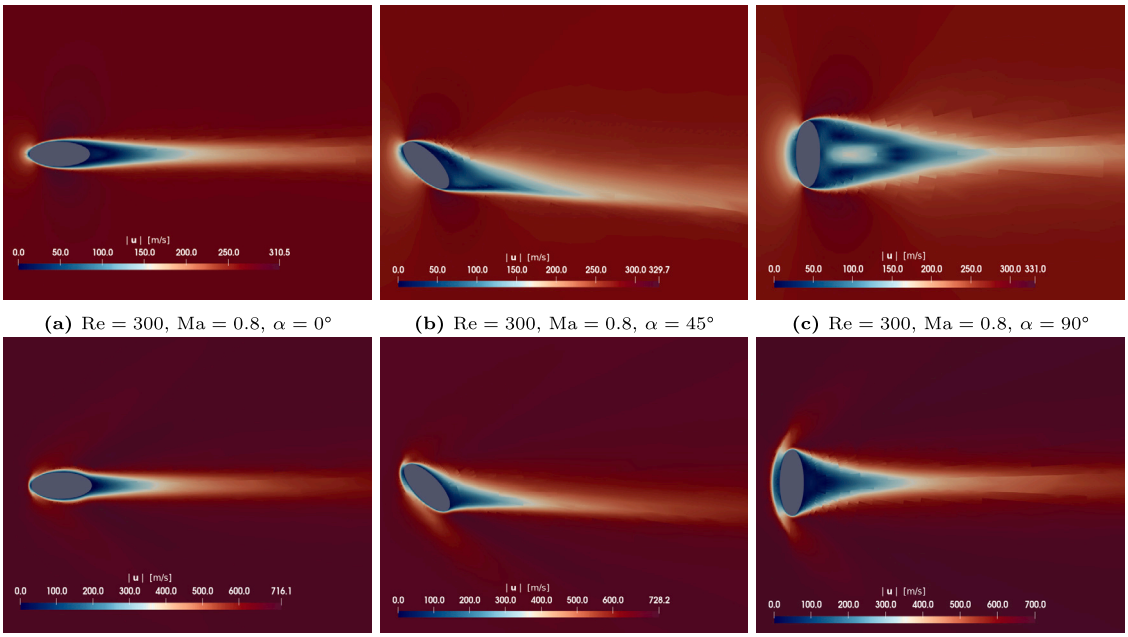

(a) Re = 300, Ma = 0.8, $\alpha = 0°$ **(b)** Re = 300, Ma = 0.8, $\alpha = 45°$ **(c)** Re = 300, Ma = 0.8, $\alpha = 90°$

(d) Re = 300, Ma = 2, $\alpha = 0°$ **(e)** Re = 300, Ma = 2, $\alpha = 45°$ **(f)** Re = 300, Ma = 2, $\alpha = 90°$

Fig. 7. Velocity fields of the prolate spheroid for Reynolds number 300, Mach numbers of 0.8 and 2 and angles of 0°, 45°, 90°.

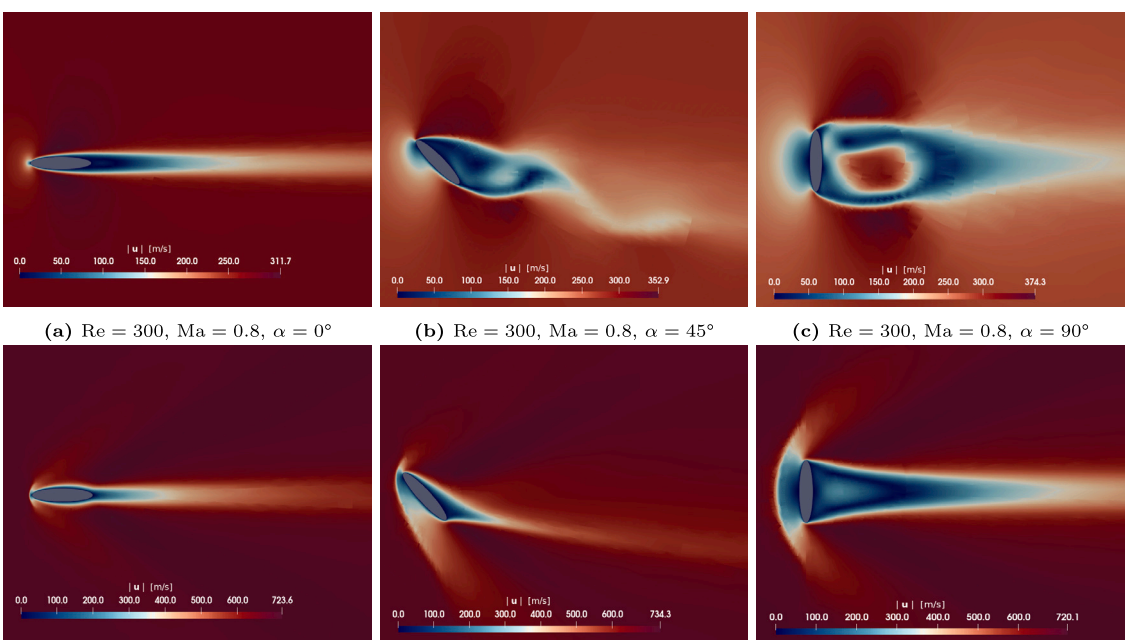

(a) Re = 300, Ma = 0.8, $\alpha = 0°$ **(b)** Re = 300, Ma = 0.8, $\alpha = 45°$ **(c)** Re = 300, Ma = 0.8, $\alpha = 90°$

(d) Re = 300, Ma = 2, $\alpha = 0°$ **(e)** Re = 300, Ma = 2, $\alpha = 45°$ **(f)** Re = 300, Ma = 2, $\alpha = 90°$

Fig. 8. Velocity fields of the oblate spheroid for Reynolds number 300, Mach numbers of 0.8 and 2 and angles of 0°, 45°, 90°.

velocity contour plots, the oblate spheroid with the strongest shock formation has the largest drag coefficients, followed by the rod-like particle, and the prolate spheroid with the weakest shock formation and the smallest drag coefficients. For all three shapes, a smaller particle Reynolds number yields a higher drag coefficient.

For all three non-spherical particle shapes, the drag coefficient in the subsonic regime increases only slightly for angles of attack of 0° to 15°, but increases more significantly as the angle of attack increases, as a function of the Mach number. For all angles of attack, the drag coefficient increases even more rapidly in the transonic regime and, afterwards, decreases in the supersonic regime. Intuition suggests that an increase in the Mach number leads to an increase in the drag coefficient, since the pressure contribution increases for high-speed flows, while the viscous contribution remains significantly smaller. However, in reality, this is only partially the case. The effect of compressibility depends on the Mach number regime of the flow. In the subsonic regime, the drag coefficient remains independent of the Mach number up to a critical Mach number, $\mathrm{Ma}_{\mathrm{cr}}$. This critical Mach number is defined as the lowest free-stream Mach number at which the flow around the particle is locally supersonic. If the free-stream Mach number is larger than $\mathrm{Ma}_{\mathrm{cr}}$, the drag coefficient starts to increase slowly. A sharp increase in the drag coefficient is observed in the transonic regime followed by a decrease in value for the supersonic regime. For a spherical particle, a similar sharp increase in the drag

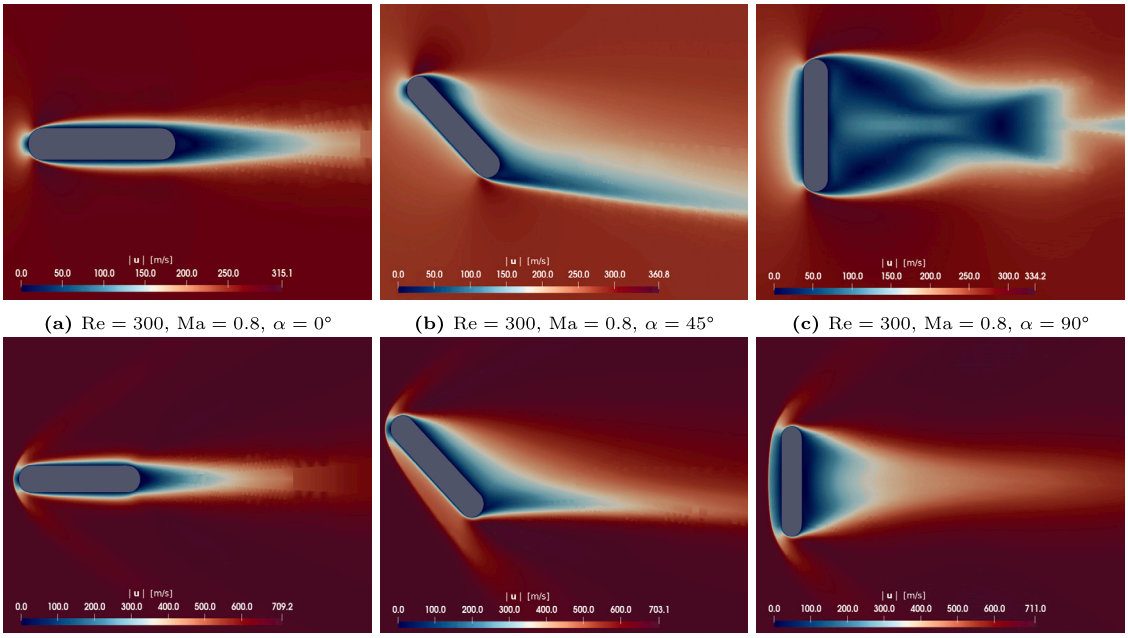

(a) $\mathrm{Re} = 300,\ \mathrm{Ma} = 0.8,\ \alpha = 0°$ **(b)** $\mathrm{Re} = 300,\ \mathrm{Ma} = 0.8,\ \alpha = 45°$ **(c)** $\mathrm{Re} = 300,\ \mathrm{Ma} = 0.8,\ \alpha = 90°$

(d) $\mathrm{Re} = 300,\ \mathrm{Ma} = 2,\ \alpha = 0°$ **(e)** $\mathrm{Re} = 300,\ \mathrm{Ma} = 2,\ \alpha = 45°$ **(f)** $\mathrm{Re} = 300,\ \mathrm{Ma} = 2,\ \alpha = 90°$

Fig. 9. Velocity fields of the rod-like particle for Reynolds number 300, Mach numbers of 0.8 and 2 and angles of 0°, 45°, 90°.

coefficient is observed for the transonic regime. However, there is little to no decline of the drag coefficient in the supersonic regimes. The sharp increase of the drag coefficient occurs when the free-stream Mach number exceeds a critical value known as the drag divergence Mach number, which marks the onset of a rapid increase in aerodynamic drag due to the formation of shock waves and compressibility effects. This termination of the supersonic flow region by a shock wave gives rise to an adverse pressure gradient. This causes a separation of the boundary layer and a dramatic increase in pressure drag (Anderson, 2003). The critical Mach number varies for different particle shapes, a blunt body such as a sphere having a relatively high critical Mach number compared to a slender body (Anderson, 2003). Moreover, the extent to which the drag coefficient decreases after the peak drag is also dependent on the Reynolds number. For a Reynolds number of 100, the drag coefficient has a steeper descent than for a Reynolds number of 300.

The lift and torque coefficients shown in Figs. B.18 and B.19 show a similar Mach number dependence as the previously analysed drag coefficient. The difference in the magnitudes of both force coefficients for different Reynolds numbers is not as large as is the case for the drag coefficient. Overall, the oblate spheroid shows the largest coefficients for lift and torque, followed by the rod-like particle and prolate spheroid. The torque coefficient has, in comparison to the drag and lift coefficients, a much steeper descent in the supersonic regime and the torque coefficients in the supersonic flow regime are even smaller compared to the coefficients in the subsonic regime.

4. Correlations for the aerodynamic force and torque coefficients

The results from the PR-DNS are used to determine the aerodynamic forces and torque, which are used to develop correlations to predict the drag, lift, and torque coefficients for each particle as a function of the particle Reynolds number, $\mathrm{Re_p}$, the Mach number, Ma, and the angle of attack between the flow and the major axis of the particle, α. The proposed correlations are all valid for a particle Reynolds number that varies in the range $100 \leq \mathrm{Re_p} \leq 300$, a Mach number of $0 \leq \mathrm{Ma} \leq 2$, and an angle of attack of $0° \leq \alpha \leq 90°$. The correlations to account for compressible effects presented in this section are extensions of the correlations of the coefficients for a particle of the same shape in an incompressible flow, for the same particle Reynolds number and angle of attack ($C_{\mathrm{D,L,M}}\left(\mathrm{Re_p}, \alpha, \mathrm{Ma} = 0\right)$). To this end, for instance, the correlations for the aerodynamic force coefficients for prolate and oblate spheroids presented by Zastawny et al. (2012) and Sanjeevi et al. (2018), and the correlations for rod-like particles of Chéron et al. (2024) and Zastawny et al. (2012) could be used as a basis for $C_{\mathrm{D,L,M}}\left(\mathrm{Re_p}, \alpha, \mathrm{Ma} = 0\right)$. This assumes that all force coefficients are constant in the range from $\mathrm{Ma} = 0$ to 0.3 for the flow conditions studied. In Appendix C a summary of the full models for all three non-spherical particles shapes are given exemplary with the correlations of Zastawny et al. (2012) for the incompressible limit. For each correlation, the fitting coefficients for a given function are estimated using curve-fitting algorithms using the Levenberg–Marquardt algorithm of the SciPy library (Johansson, 2019). The accuracy of the new correlations are assessed by calculating the maximum and median errors of their prediction, ϵ_{max} and ϵ_{med}. The error in the prediction is defined as

$$\epsilon_i = \frac{\|f_{\mathrm{corr},i} - f_{\mathrm{PR-DNS},i}\|}{\max\left(\|f_{\mathrm{corr},i}\|, \|f_{\mathrm{PR-DNS},i}\|\right)}, \tag{9}$$

where $f_{\mathrm{PR-DNS},i}$ represents the value of a given force or torque coefficient from the ith PR-DNS simulation, and $f_{\mathrm{corr},i}$ is the value predicted by the correlation for the given force or torque coefficient. The prediction error is scaled by the maximum value between the coefficient prediction by the curve fitting algorithms and the PR-DNS value because the force coefficient can be zero. This zero value occurs for the lift and torque coefficients of a particle with an angle of attack of $\alpha = 0°$ or 90°. The fitting coefficients given in Tables 1–3 are rounded to three significant figures for readability, exact values are given in the attached data repository.

4.1. Drag coefficient

The proposed correlation for the drag coefficient of each studied particle shape is based on the drag coefficient in the incompressible

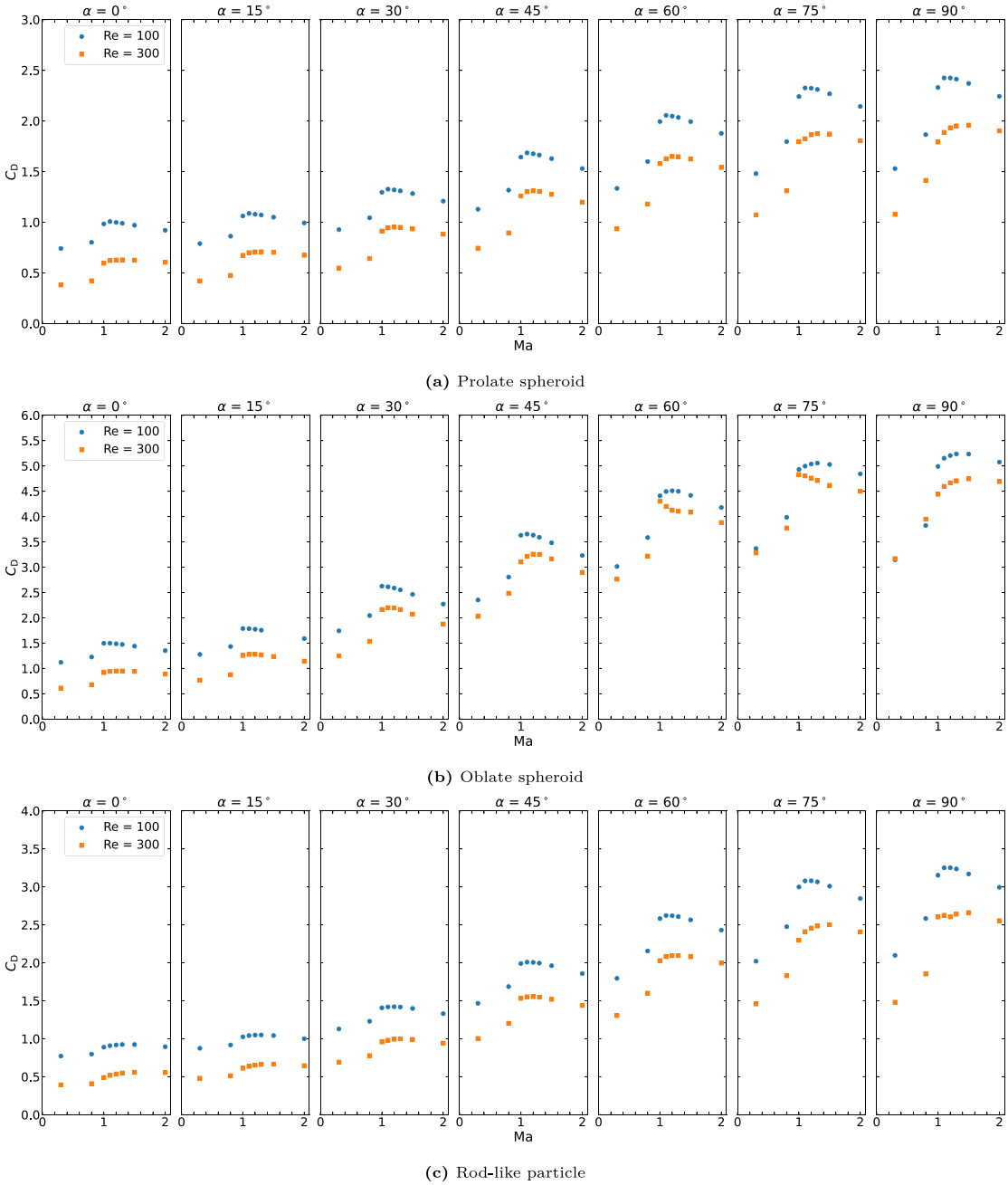

(a) Prolate spheroid

(b) Oblate spheroid

(c) Rod-like particle

Fig. 10. Variation of the drag coefficient C_D with Mach number Ma for different angles of attack considered for the three considered non-spherical particle shapes.

flow regime and a compressible correction that is a function of the particle Reynolds number, the Mach number, and the angle of attack. The general expression is defined as

$$C_D\left(\mathrm{Re_p}, \alpha, \mathrm{Ma}\right) = C_D\left(\mathrm{Re_p}, \alpha, \mathrm{Ma}=0\right)\left[1 + \mathcal{F}_D^{\mathrm{Ma}}\left(\mathrm{Re_p}, \alpha, \mathrm{Ma}\right)\right] \tag{10}$$

where C_D is the drag coefficient of a specific particle given as a function of the particle Reynolds number, angle of attack, and Mach number. This coefficient depends on the drag coefficient for equivalent particle Reynolds number and angle of attack in incompressible flow conditions, and an additional shape-dependent function, $\mathcal{F}_D^{\mathrm{Ma}}$ to account for the change in the coefficient as a result of the compressibility of the flow. The expressions of these shape-dependent functions are given in the dedicated sections, along with the associated prediction errors. The fitting coefficients, ϑ_i, for the drag coefficients of all three considered particle shapes are given in Table 1.

4.1.1. *Prolate spheroid*

To consider compressible effects in the prediction of the drag coefficient of an isolated prolate spheroid particle, the shape-dependent function, $\mathcal{F}_D^{\mathrm{Ma}}$, in Eq. (10) is given by

$$\mathcal{F}_D^{\mathrm{Ma}}\left(\mathrm{Re_p}, \alpha, \mathrm{Ma}\right) = \frac{\left(\vartheta_1 \mathrm{Re_p} + \vartheta_2 \alpha^{\vartheta_3}\right)}{\left[1 + \exp\left(-\vartheta_4(\mathrm{Ma} - \vartheta_5)\right)\right]} + \vartheta_6 \exp\left(-\frac{(\mathrm{Ma} - \vartheta_7)^2}{\vartheta_8}\right). \tag{11}$$

The first term on the right hand-side of Eq. (11) captures the sigmoid evolution of the drag coefficient as the Mach number transitions from the subsonic to the supersonic flow regime, where two plateaus are observed. In the transonic region, there is a noticeable increase in the drag coefficient, forming a bell-shaped peak. This peak, caused by the transition from subsonic to supersonic flow, is captured with the second term on the right-hand side of Eq. (11) that is modelled based

Table 1
List of the fitting coefficients in Eqs. (11), (12), and (13), used in the correlation to predict the change in the drag coefficient in the case of compressible flow.

	ϑ_1	ϑ_2	ϑ_3	ϑ_4	ϑ_5	ϑ_6	ϑ_7	ϑ_8	ϑ_9	ϑ_{10}	ϑ_{11}
Eq. (11)	1.55×10^{-3}	0.201	0.492	15.6	0.878	0.183	1.21	0.142	–	–	–
Eq. (12)	6.07	0.269	4.40×10^{-5}	2.10	3.90	21.3	0.853	0.130	1.17	0.252	–
Eq. (13)	1.14×10^{-3}	0.121	2.64	0.0983	1.40	14.6	0.861	3.94	0.631	1.20	0.330

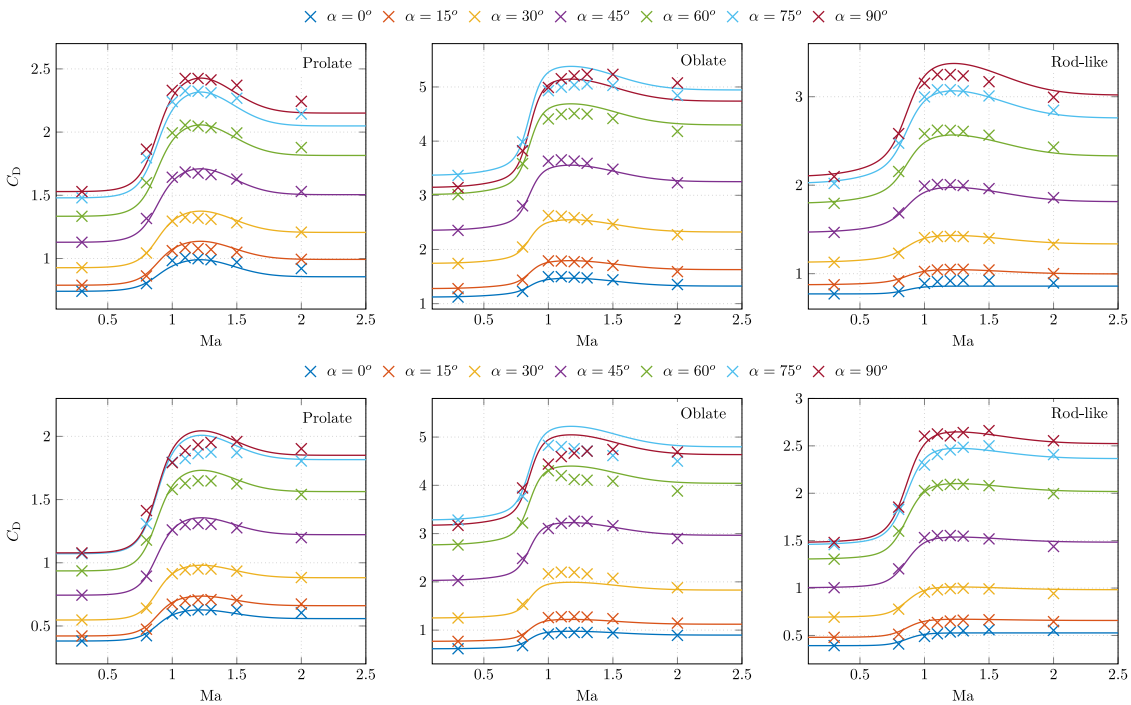

Fig. 11. The drag coefficient as a function of the Mach number for the three shapes studied, at different particle Reynolds numbers, for all considered angles of attack. From left column to right column: prolate spheroid, oblate spheroid, and rod-like particle. Top row: $\mathrm{Re_p} = 100$, bottom row: $\mathrm{Re_p} = 300$. The colour indicates the angle of attack, the marker indicates PR-DNS result, and the solid line shows the prediction of the drag coefficient given by the derived correlations, Eqs. (11), (12), and (13).

on a Gaussian function. Both terms vary as a function of the particle Reynolds number and the angle of attack; the closer the angle of attack is to $\alpha = 90°$, the larger is the change in the drag coefficient.

The PR-DNS results along with the correlation for the prediction of the drag coefficient of the prolate spheroid are shown in the left of Fig. 11, as a function of the Mach number, for all angles of attack and particle Reynolds number values considered in this work. The correlation accurately recovers the change in the evolution of the drag coefficient in both transonic and supersonic regimes, for all particle Reynolds numbers and angles of attack. The maximum and median prediction errors between the correlation and the PR-DNS are 7.56% and 1.77%, respectively.

4.1.2. Oblate spheroid

To consider compressible effects in the prediction of the drag coefficient of an isolated oblate spheroid particle, the shape-dependent function, $\mathcal{F}_{\mathrm{D}}^{\mathrm{Ma}}$, in Eq. (10) is given by

$$\mathcal{F}_{\mathrm{D}}^{\mathrm{Ma}}\left(\mathrm{Re_p}, \alpha, \mathrm{Ma}\right) = \frac{\vartheta_1/\log(\mathrm{Re_p})\left(\vartheta_2\alpha/\pi\right)^{\vartheta_3(\mathrm{Re_p})^{\vartheta_4}} + \log(\mathrm{Re_p})/\vartheta_5 - 1}{\left[1 + \exp\left(-\vartheta_6(\mathrm{Ma} - \vartheta_7)\right)\right]} + \vartheta_8 \exp\left(-\frac{(\mathrm{Ma} - \vartheta_9)^2}{\vartheta_{10}}\right). \tag{12}$$

The purpose of the first term on the right hand-side of Eq. (12) is similar to the model for the prolate spheroid, it captures the sigmoid evolution of the drag coefficient as the Mach number increases from subsonic to supersonic regimes. However, in the case of the oblate spheroid, at high particle Reynolds number, the drag coefficient is no longer largest at $\alpha = 90°$. This is modelled by a modification of the term multiplying the Reynolds number and the angle of attack in Eq. (12). The remainder of the expression is similar to the expression given for the prolate spheroid, where the second term on the right hand side also models the smooth increase in the evolution of the drag coefficient in the transonic regime.

The correlation for the prediction of the drag coefficient for the oblate spheroid is shown in the centre of Fig. 11, along with the PR-DNS results. For all angles of attack, except for $\alpha = 75°$, the correlation accurately recovers the change in the evolution of the drag coefficient in both the transonic and supersonic regimes, for all particle Reynolds numbers. For $\alpha = 75°$, the variation in the difference between the value of the drag coefficient in the subsonic and supersonic regimes deviates from other angles and remains challenging to capture. However, a very good agreement is observed as the maximum and median prediction errors between the correlation and the PR-DNS are 10.19% and 2.1%, respectively.

4.1.3. Rod-like particle

For the rod-like particle, the shape-dependent function $\mathcal{F}_{\mathrm{D}}^{\mathrm{Ma}}$, in Eq. (10), used to model compressible effects, is given by

$$\mathcal{F}_{\mathrm{D}}^{\mathrm{Ma}}\left(\mathrm{Re_p}, \alpha, \mathrm{Ma}\right) = \frac{\vartheta_1 \cdot \mathrm{Re_p} + \vartheta_2 \cdot \left(\frac{\mathrm{Re_p}}{\vartheta_3}\right)^{\vartheta_4} \cdot \alpha^{\vartheta_5}}{\left[1.0 + \exp\left(-\vartheta_6 \cdot (\mathrm{Ma} - \vartheta_7)\right)\right]} + \left(\frac{\vartheta_8 \cdot \alpha}{\mathrm{Re_p}}\right)^{\vartheta_9} \cdot \exp\left(-\frac{(\mathrm{Ma} - \vartheta_{10})^2}{\vartheta_{11}}\right) \tag{13}$$

The first term on the right hand-side of Eq. (13) is similar to the expression given for the prolate spheroid, Eq. (11), as the observations are

Table 2
List of the fitting coefficients in Eqs. (15), (18), and (19), used in the correlation to predict the change in the lift coefficient in case of compressible flow.

	ϑ_1	ϑ_2	ϑ_3	ϑ_4	ϑ_5	ϑ_6	ϑ_7	ϑ_8
Eq. (15)	1.17	−0.735	−21.8	0.870	0.277	1.12	0.217	2.00
Eq. (18)	0.535	130	0.807	1.84	1.56	−0.996	2.25	0.516
Eq. (19)	2.43	1.20	−24.8	0.807	2.43	1.24	0.237	4.22

the same. The larger is the angle of attack, the larger is the difference between the drag coefficient in the subsonic and the supersonic flow regimes. However, the second term on the right hand-side of Eq. (13), which is also based on a Gaussian function, is scaled by the angle of attack. The rationale is that, for the rod-like particle, the bell shape that represents the change in the drag coefficient in the transonic regime is less pronounced for angles of attack close to $\alpha \to 0°$, and is not present for a rod-like particle with an angle of attack $\alpha = 0°$. This is shown in the right of Fig. 11, depicting the prediction of the drag coefficient of the rod-like particle with the correlation along with the PR-DNS results. For all flow cases, a good agreement is observed between the predictions and the PR-DNS results as a maximum and median prediction errors between the correlation and the PR-DNS are 7.06% and 1.29%, respectively.

4.2. Lift coefficient

Following a similar approach as for the drag coefficients, the proposed correlation for the lift coefficient of each studied particle shape is based on the lift coefficient in the incompressible flow regime and a compressible correction that is a function of the particle Reynolds number, the Mach number, and the angle of attack. The general expression is defined as

$$C_L\left(\mathrm{Re_p}, \alpha, \mathrm{Ma}\right) = C_L\left(\mathrm{Re_p}, \alpha, \mathrm{Ma} = 0\right) + \mathcal{F}_L^{\mathrm{Ma}}\left(\mathrm{Re_p}, \alpha, \mathrm{Ma}\right) \tag{14}$$

where C_L is the lift coefficient of a specific particle given as a function of the particle Reynolds number, angle of attack, and Mach number. This coefficient is obtained from the summation of the lift coefficient for equivalent particle Reynolds number and angle of attack in incompressible flow conditions, and an additional shape-dependent function, $\mathcal{F}_L^{\mathrm{Ma}}$, to account for the change in the lift coefficient in case of compressible flow. The expressions of the shape-dependent function $\mathcal{F}_L^{\mathrm{Ma}}$ are given in the dedicated sections, along with the associated prediction errors. The fitting coefficients, ϑ_i, for the lift coefficients of all three considered particle shapes are given in Table 2.

4.2.1. Prolate spheroid

To consider compressible effects in the prediction of the lift coefficient of an isolated prolate spheroid particle, the shape-dependent function, $\mathcal{F}_L^{\mathrm{Ma}}$, in Eq. (14), is given by

$$\begin{aligned}\mathcal{F}_L^{\mathrm{Ma}}\left(\mathrm{Re_p}, \alpha, \mathrm{Ma}\right) = &\frac{\vartheta_1 \log\left(\mathrm{Re_p}\right)^{\vartheta_2}}{\left[1 + \exp\left(\vartheta_3(\mathrm{Ma} - \vartheta_4)\right)\right]} \cos\left(\Psi_1\left(\alpha, \mathrm{Re_p}\right)\right) \sin\left(\Psi_1\left(\alpha, \mathrm{Re_p}\right)\right) \\ &+ \vartheta_5 \exp\left(\frac{-(\mathrm{Ma} - \vartheta_6)^2}{\vartheta_7}\right) \left[\cos\left(\Psi_2\left(\alpha, \mathrm{Re_p}\right)\right) \sin\left(\Psi_2\left(\alpha, \mathrm{Re_p}\right)\right)\right]^{\vartheta_8}.\end{aligned} \tag{15}$$

As for the drag correlation derived for the prolate spheroid, Eq. (11), the correlation to predict the lift coefficient is split in two terms: a sigmoid term to model the change in the lift coefficient from subsonic to supersonic regimes, and a Gaussian function to model the smooth bell-shaped evolution of the coefficient from the subsonic to the supersonic flow regime. These two terms are multiplied by a cosine–sine factor so that the lift coefficients remain equal to $C_L = 0$ for a prolate particle with angles of attack $\alpha = 0°$ and 90°, and maximum for $\alpha = 45°$. It is important to mention that for finite particle Reynolds numbers, such as those considered in the present study, the lift coefficient is no longer largest for a particle with an angle of attack of $\alpha = 45°$ (Fröhlich et al., 2020; Sanjeevi et al., 2022; Chéron et al., 2024). This is also observed in this work and shifting functions are used to model the change in the maximum value of the lift coefficient as a function of the angle of attack. These functions are given by

$$\Psi_1 = \frac{\pi}{2}\left(\alpha\frac{2}{\pi}\right)^{1+4.185\times10^{-5}\log\left(\mathrm{Re_p}\right)^{-10.5}} \tag{16}$$

for the first cosine–sine term in Eq. (15) and

$$\Psi_2 = \frac{\pi}{2}\left(\alpha\frac{2}{\pi}\right)^{1+2.146\log\left(\mathrm{Re_p}\right)^{-1.444}} \tag{17}$$

for the second cosine–sine term in Eq. (15).

The PR-DNS results along with the correlation for the prediction of the lift coefficient of the prolate spheroid are shown in the left of Fig. 12, as a function of the Mach number, for all angles of attack and particle Reynolds number values considered in this work. The correlation accurately recovers the evolution of the lift coefficient in all regimes, for all particle Reynolds numbers and angles of attack. The maximum and median prediction errors between the correlation and the PR-DNS are 13.93% and 0.72%, respectively.

4.2.2. Oblate spheroid

For the oblate spheroid, the shape-dependent function, $\mathcal{F}_L^{\mathrm{Ma}}$, in Eq. (14), is given by

$$\begin{aligned}\mathcal{F}_L^{\mathrm{Ma}}\left(\mathrm{Re_p}, \alpha, \mathrm{Ma}\right) = &\frac{\vartheta_1 \log(\mathrm{Re_p})}{\left[1 + \exp\left(-\vartheta_2(\mathrm{Ma} - \vartheta_3)\right)\right]} \cos(\alpha)^{\vartheta_4} \sin(\alpha)^{\vartheta_5} \\ &+ \vartheta_6 \exp\left(-\frac{(\mathrm{Ma} - \vartheta_7)^2}{\vartheta_8}\right) \cos(\alpha)\sin(\alpha).\end{aligned} \tag{18}$$

The results of the evolution of the lift coefficient as a function of the angle of attack for the oblate spheroid, see the centre of Fig. 12, show that the values for the lift coefficients are almost symmetric with respect to the angle of attack $\alpha = 45°$. This trend indicates that the shift in the angle of attack at which the maximum lift coefficient occurs is less influenced by the increase in the particle Reynolds number than for the rod-like and the prolate spheroid particles. The specific evolution of the lift coefficient that varies from the other shapes confirms the necessity to have a unique correlation to predict the lift coefficient. This unique modification relies on the change of the exponent in the cosine–sine multiplication, realized by the exponents ϑ_4 and ϑ_5. In general, the correlation agrees well with the PR-DNS results, as the maximum and median prediction errors between the correlation and the PR-DNS are 13.66% and 0.19%, respectively.

4.2.3. Rod-like particle

To consider compressible effects in the prediction of the lift coefficient of an isolated rod-like particle, the shape-dependent function, $\mathcal{F}_L^{\mathrm{Ma}}$, in Eq. (14), is given by

$$\begin{aligned}\mathcal{F}_L^{\mathrm{Ma}}\left(\mathrm{Re_p}, \alpha, \mathrm{Ma}\right) = &\frac{\left(\vartheta_1/\log\left(\mathrm{Re_p}\right)\right)^{\vartheta_2}}{\left[1 + \exp\left(\vartheta_3 \cdot (\mathrm{Ma} - \vartheta_4)\right)\right]} \cos\left(\Psi_1\left(\alpha, \mathrm{Re_p}\right)\right) \sin\left(\Psi_1\left(\alpha, \mathrm{Re_p}\right)\right) \\ &+ \vartheta_5 \exp\left(\frac{-(\mathrm{Ma} - \vartheta_6)^2}{\vartheta_7}\right) \left[\cos\left(\Psi_2\left(\alpha, \mathrm{Re_p}\right)\right) \sin\left(\Psi_2\left(\alpha, \mathrm{Re_p}\right)\right)\right]^{\vartheta_8}.\end{aligned} \tag{19}$$

This expression is similar to the expression proposed to model the lift coefficient of the prolate spheroid, Eq. (19), the correlation to predict the lift coefficient is split in the sigmoid term, for the transition from the subsonic to the supersonic flow regime, and the Gaussian function term for the bump in the transonic regime. These two terms are multiplied by a cosine–sine factor, where the angle of attack is modified using shifting functions to model the change in the maximum value of the

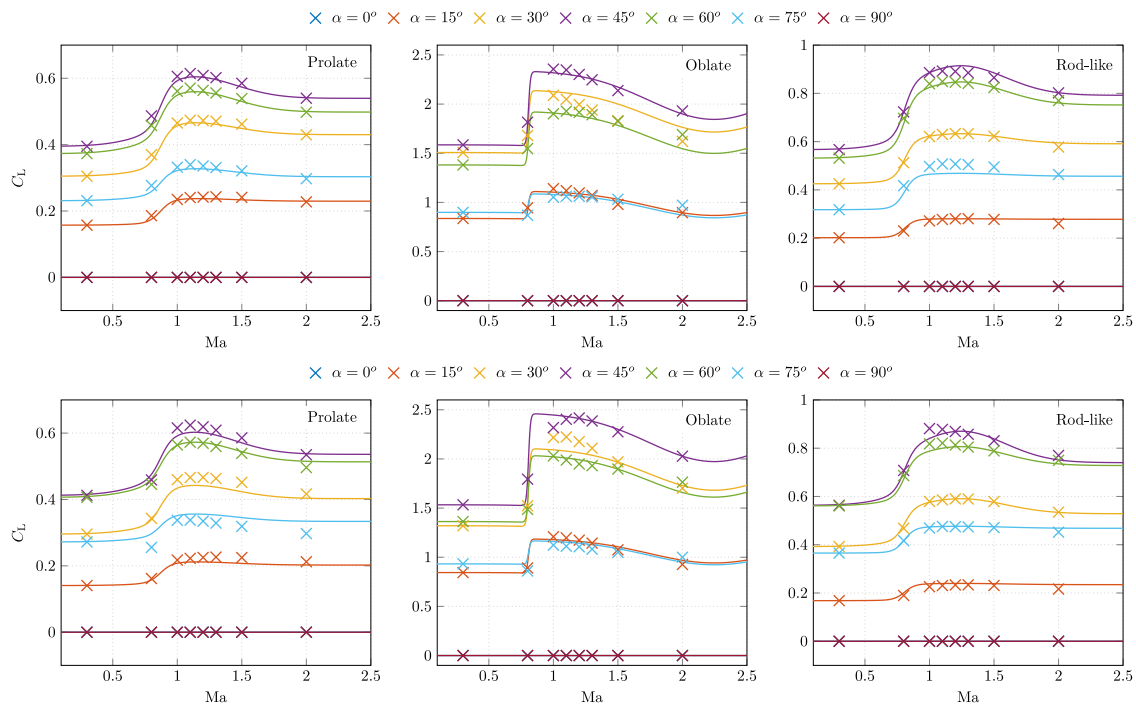

Fig. 12. The lift coefficient as a function of the Mach number for the three shapes studied, at different particle Reynolds numbers, for all considered angles of attack. From left column to right column: prolate spheroid, oblate spheroid, and rod-like particle. Top row: $\mathrm{Re_p} = 100$, bottom row: $\mathrm{Re_p} = 300$. The colour indicates the angle of attack, the marker indicates PR-DNS result, and the solid line shows the prediction of the lift coefficient given by the derived correlations, Eqs. (15), (18), and (19).

lift coefficient as a function of the angle of attack (Chéron et al., 2024). These functions are given by

$$\Psi_1 = \frac{\pi}{2}\left(\alpha\frac{2}{\pi}\right)^{1+2.471\log\left(\mathrm{Re_p}\right)^{-1.50}} \tag{20}$$

for the first cosine–sine term in Eq. (19) and

$$\Psi_2 = \frac{\pi}{2}\left(\alpha\frac{2}{\pi}\right)^{1+1630.79\left(1/\log\left(\mathrm{Re_p}\right)\right)^{6.00}} \tag{21}$$

for the second cosine–sine term in Eq. (19).

The PR-DNS results along with the correlation for the prediction of the rod-like particle lift coefficient are shown in the right plot of Fig. 12, as a function of the Mach number, for all angles of attack and particle Reynolds number values considered in this work. The correlation accurately recovers the evolution of the lift coefficient in all regimes, for all particle Reynolds numbers and angles of attack. The maximum and median prediction errors between the correlation and the PR-DNS are 7.97% and 0.15%, respectively.

4.3. Torque coefficient

As for the drag and lift coefficients, the proposed correlation for the torque coefficient of each studied particle shape is based on the torque coefficient in the incompressible flow regime and a compressible correction that is a function of the particle Reynolds number, the Mach number, and the angle of attack. The general expression is defined as

$$C_\mathrm{M}\left(\mathrm{Re_p},\alpha,\mathrm{Ma}\right) = C_\mathrm{M}\left(\mathrm{Re_p},\alpha,\mathrm{Ma}=0\right) + \mathcal{F}_\mathrm{M}^\mathrm{Ma}\left(\mathrm{Re_p},\alpha,\mathrm{Ma}\right) \tag{22}$$

where C_M is the torque coefficient of a specific particle given as a function of the particle Reynolds number, the Mach number, and the angle of attack. This coefficient is obtained from the summation of the torque coefficient for equivalent particle Reynolds number and angle of attack in incompressible flow conditions, and an additional shape-dependent function, $\mathcal{F}_\mathrm{M}^\mathrm{Ma}$, to account for the change in the torque coefficient in case of compressible flow. For all shapes, the evolution of the torque coefficient as a function of the Mach number is very similar, so that the general expression of the shape-dependent function is unique, and given by

$$\mathcal{F}_\mathrm{M}^\mathrm{Ma} = \frac{\vartheta_1\mathrm{Re_p} + \vartheta_2\left(\mathrm{Re_p}/\vartheta_3\right)^{\vartheta_4}}{1+\exp\left(-\vartheta_5\left(\mathrm{Ma}-\vartheta_6\right)\right)}\cdot\left(\cos\left(\Psi_1\right)\sin\left(\Psi_1\right)\right)^{\vartheta_7} + \left(\frac{\vartheta_8\alpha}{\vartheta_{10}}\right)^{\vartheta_9}\cdot\left(\frac{\vartheta_{11}\mathrm{Re_p}}{\vartheta_{13}}\right)^{\vartheta_{12}}\cdot\exp\left(\frac{-\left(\mathrm{Ma}-\vartheta_{14}\right)^2}{\vartheta_{15}}\right)\cdot\left(\cos\left(\Psi_2\right)\sin\left(\Psi_2\right)\right)^{\vartheta_{16}}, \tag{23}$$

with the functions to shift the maximum value of the cosine–sine product given as

$$\Psi_1 = \frac{\pi}{2}\left(\alpha\frac{2}{\pi}\right)^{\vartheta_{17}}, \tag{24}$$

and

$$\Psi_2 = \frac{\pi}{2}\left(\alpha\frac{2}{\pi}\right)^{\vartheta_{18}}. \tag{25}$$

As for the drag and lift correlations, the correlation to predict the torque coefficient is split in two main terms: the sigmoid term to model the change in the torque coefficient from subsonic to supersonic regimes, and a Gaussian function to model the smooth evolution of the coefficient from the subsonic to the supersonic flow regime. Both terms are multiplied by a shifted cosine–sine factor so that the torque coefficients remain zero for the angles of attack $\alpha = 0°$ and $\alpha = 90°$, and to model the shift in the maximum torque coefficient. The fitting coefficients, ϑ_i, for the torque coefficients of all three considered particle shapes are given in Table 3. The results of the PR-DNS along with the correlation for the torque coefficient of the prolate spheroid are shown in the left of Fig. 13, as a function of the Mach number, for

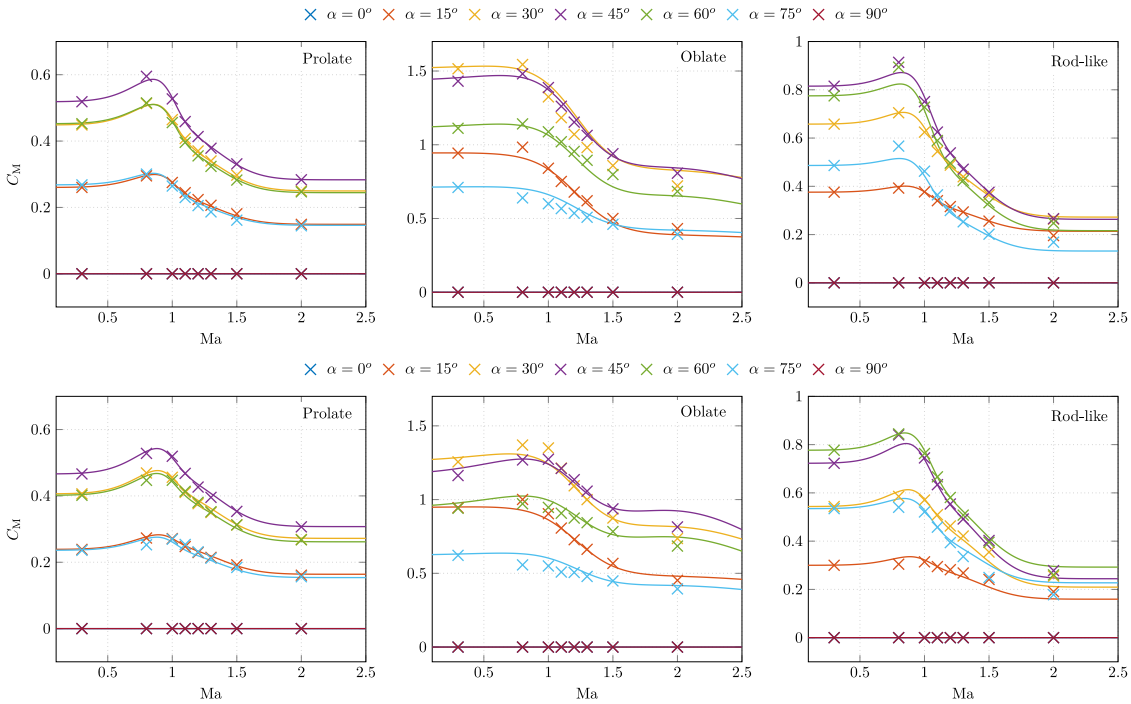

Fig. 13. The torque coefficient as a function of the Mach number for the three shapes studied, at different particle Reynolds numbers, for all considered angles of attack. From left column to right column: prolate spheroid, oblate spheroid, and rod-like particle. Top row: Re_p = 100, bottom row: Re_p = 300. The colour indicates the angle of attack, the marker indicates PR-DNS result, and the solid line shows the prediction of the torque coefficient given by the derived correlations, Eqs. (23), (24), and (25).

all angles of attack and particle Reynolds number values considered in this work. The change from the subsonic to the supersonic flow regimes is accurately recovered for all considered angles of attack and particle Reynolds numbers by the sigmoid term, leading to maximum and median prediction errors between the correlation and the PR-DNS of 6.88% and 0.44%, respectively. As for the prolate spheroid, the model prediction for the torque coefficient of the oblate spheroid is shown with the PR-DNS results in the centre of Fig. 13. The evolution of the torque coefficient of the oblate spheroid is very similar compared with the prolate spheroid and the correlation accurately recovers the smooth transition from the subsonic to the supersonic flow regime, leading to maximum and median prediction errors between the correlation and the PR-DNS of 12.96% and 1.40%, respectively. For the rod-like particle, the model prediction for the torque coefficient is shown against the PR-DNS results in the right of Fig. 13. In this case, the transition from subsonic to supersonic flow regime is much more significant compared to the other two particle shapes and the PR-DNS results in the transition region are more narrow, which makes it more difficult to find an accurate model prediction. Hence, the maximum prediction error between the correlation and the PR-DNS is 22.40% because of a single outlier, but the median prediction error is 0.18%, which shows that the correlation is over all in an excellent agreement with the PR-DNS results.

5. Conclusions

In this study, we have presented particle-resolved direct numerical simulations (PR-DNS) with three-dimensional body-fitted hexahedral meshes to investigate the aerodynamic force and torque coefficients of particles with different shapes, using a finite-volume-based solver for compressible flows. The employed computational domain is spherical, centred around the particle, facilitating the rotation of the particle without changing the computational mesh. This computational domain is represented by non-uniform and body-conforming meshes, refined near the particle. PR-DNS are carried out for three particle shapes, namely a prolate spheroid with an aspect ratio of 5/2, an oblate spheroid with an aspect ratio of 5, and a rod-like particle with an aspect ratio of 5. The simulations are carried out at a reference temperature of 300 K and a reference pressure of 10^5 Pa, maintaining a Prandtl number of 0.71.

Table 3
List of the fitting coefficients in Eqs. (23), (24), and (25), used in the correlation to predict the change in the torque coefficient in case of compressible flow.

	Prolate	Oblate	Rod-like
ϑ_1	2.28×10^{-4}	-4.43×10^{-3}	-2.32×10^{-5}
ϑ_2	−0.444	−0.759	−1.15
ϑ_3	157	203	127
ϑ_4	−0.223	−1.03	−0.134
ϑ_5	15.1	5.93	12.3
ϑ_6	1.01	1.22	1.03
ϑ_7	0.993	1.11	1.04
ϑ_8	4.96×10^{-2}	3.18×10^{-9}	13.8
ϑ_9	1.44	8.95×10^{-2}	1.88
ϑ_{10}	7.42×10^{-3}	3.59×10^{-2}	3.64
ϑ_{11}	3.81×10^{-2}	3.89	0.520
ϑ_{12}	1.68×10^{-2}	0.569	0.158
ϑ_{13}	5.86×10^{-9}	10.8	1.22×10^{-6}
ϑ_{14}	1.10	1.98	1.18
ϑ_{15}	9.29×10^{-3}	1.04	3.71×10^{-3}
ϑ_{16}	1.05	2.50	1.16
ϑ_{17}	0.164	1.17	0.157
ϑ_{18}	1.04	0.809	1.32

This study has examined the behaviour of non-spherical particles in compressible flows, focusing on the steady-state velocity as well as the aerodynamic force coefficients (drag, lift, and torque) for the three considered particle shapes at Mach numbers ranging from 0.3 to

2.0, angles of attack from 0° to 90°, and particle Reynolds numbers between 100 and 300. The bow shock developing in the supersonic flow regime in front of the particle is largest for the oblate spheroid and smallest for the prolate spheroid. In the transonic regime, the oblate spheroid exhibits an unstable wake behaviour when the angle of attack is larger than 0°. The drag coefficients increase with the angle of attack and are highest for the oblate spheroid. All shapes show a rapid increase in drag in the transonic regime, followed by a decrease in the supersonic regime. The lift and torque coefficients follow similar trends, with the oblate spheroid having the highest values. We can, therefore, conclude that the shape of the particles impacts the flow behaviour and aerodynamic forces significantly, with oblate spheroids showing the most pronounced effects due to their geometric characteristics.

The correlations proposed in this work are valid for particle Reynolds numbers between 100 and 300, Mach numbers between 0 and 2, and angles of attack ranging from 0° to 90°. The correlations accurately recover the change in the evolution of the aerodynamic force and torque coefficients in both transonic and supersonic regimes, for all considered particle Reynolds numbers and angles of attack. The largest maximum error of the correlations for the drag coefficient is 10.19% for the prolate spheroid, while the median error for the three considered particle shapes is approximately 1%–2%. The proposed correlations for the lift coefficient have a slightly larger maximum error, with the prolate particle correlation having the highest maximum error of 13.93%. However, the median error of the correlations for the lift coefficient is below 1% which highlights the overall excellent accuracy. For the torque coefficient, the correlation of the rod-like particle has the largest maximum error with 22.4%. Again, the median error of the torque correlations for all three particles shapes is approximately 1%, which indicates that the relatively high maximum error comes from a single outlier, but the overall correlations are in excellent agreement.

The development and validation of aerodynamic force and torque correlations for non-spherical particles in compressible flows mark a significant advancement in the field of multiphase flow modelling. By providing accurate and tailored correlations, this work addresses the long-standing challenge of representing the complex behaviour of non-spherical particles under varying and compressible flow conditions. The new correlations will, for example, enhance the precision of point-particle simulations, enabling more reliable predictions of particle-laden flow dynamics for compressible flow regimes.

While our current study focuses on oblate spheroids, prolate spheroids, and rod-like particles, these shapes serve as idealized cases that span a range of aspect ratios and flow characteristics. For particles with shapes that deviate from these categories, various approaches could be considered. One possibility could be the interpolation between the correlations. If the particle shape is approximately spheroidal or rod-like but does not fit perfectly within our definitions, users might interpolate between the aerodynamic force coefficients for oblate, prolate, and rod-like shapes based on the particle aspect ratio and geometry. For irregular or non-standard shapes, the methodology used in this study (e.g., using numerical simulations or experimental data) could be extended to derive additional correlations for those shapes. Alternatively, a shape factor or a drag coefficient correction based on empirical or computational approaches could be applied. Users may also combine our correlations with existing generalized drag or force models that account for irregular particle shapes through empirical shape factors or coefficients.

CRediT authorship contribution statement

Christian Gorges: Writing – review & editing, Writing – original draft, Software, Visualization, Validation, Investigation, Formal analysis, Data curation. **Victor Chéron:** Writing – original draft, Software, Investigation, Data curation. **Anjali Chopra:** Writing – review & editing, Formal analysis, Data curation. **Fabian Denner:** Writing – review & editing, Supervision, Software, Methodology, Investigation, Funding acquisition, Formal analysis, Conceptualization. **Berend van Wachem:** Writing – review & editing, Supervision, Software, Resources, Project administration, Methodology, Investigation, Funding acquisition, Formal analysis, Data curation, Conceptualization.

Declaration of competing interest

The authors declare that they have no known competing financial interests or personal relationships that could have appeared to influence the work reported in this paper.

Acknowledgements

This research was funded by the Deutsche Forschungsgemeinschaft (DFG, German Research Foundation), Germany - Project-ID 447633787. We would like to express our sincere gratitude to the reviewers for their insightful comments and valuable suggestions, which have significantly contributed to improving the quality of this manuscript.

Appendix A. Mesh convergence study

In this appendix we give the mesh convergence studies for the three non-spherical particle shapes. For each shape the convergence behaviour of the drag coefficient is shown for $\mathrm{Re} = 300$, $\alpha = 0$ and Ma of 0.3 and 2. A coarse and a medium mesh with and without static adaptive mesh refinement (AMR) (see Fig. A.14) in the area of interest are compared to a fine mesh. In Figs. A.15–A.17, the crosses represent the results for a coarse base mesh with optional static AMR in the area of interest around the particle and its wake. One and two levels of static AMR refinement mean that the initial coarse cells in the area of interest are subdivided once or twice, resulting in a finer mesh where needed. The circles represent a medium mesh with optional static AMR and the filled circle represent a very fine mesh as a reference.

Appendix B. Lift and torque coefficient diagrams

In this appendix we give the diagrams for the variation of the lift and torque coefficients with the Mach number for different angles of attack. Figs. B.18 and B.19 present the lift coefficients, C_{L}, and the torque coefficients, C_{M}, respectively, for all three non-spherical particle

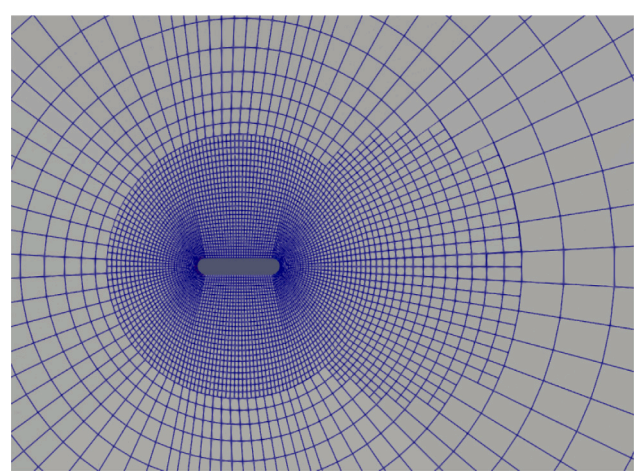

Fig. A.14. Example of a static AMR mesh, showing the mesh refinement in the area of interest around the particle and its wake.

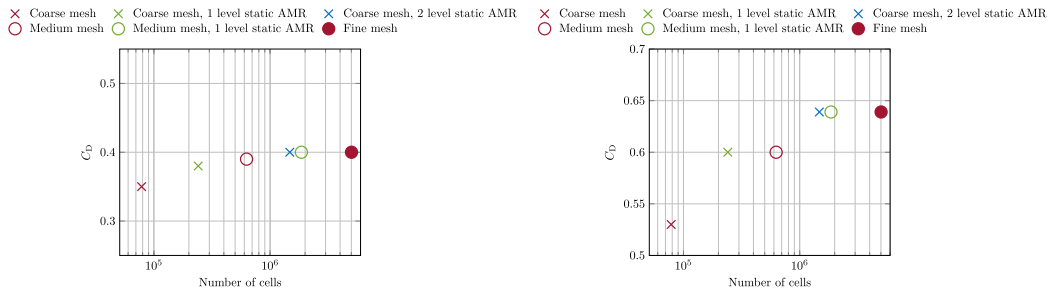

(a) Re = 300, Ma = 0.3, $\alpha = 0°$ **(b)** Re = 300, Ma = 2.0, $\alpha = 0°$

Fig. A.15. Convergence behaviour of the drag coefficient for a prolate spheroid particle.

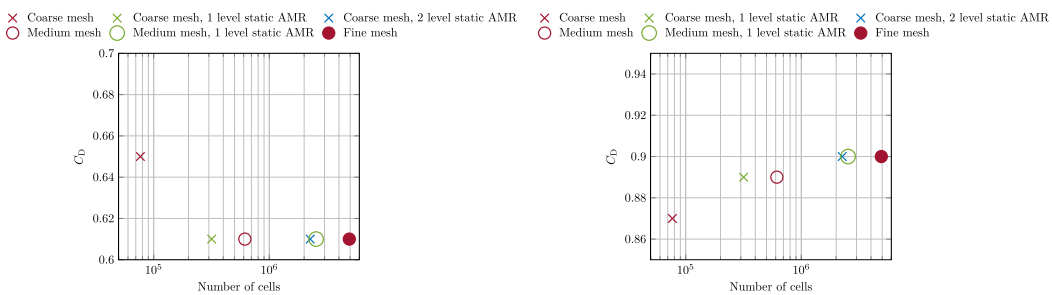

(a) Re = 300, Ma = 0.3, $\alpha = 0°$ **(b)** Re = 300, Ma = 2.0, $\alpha = 0°$

Fig. A.16. Convergence behaviour of the drag coefficient for a oblate spheroid particle.

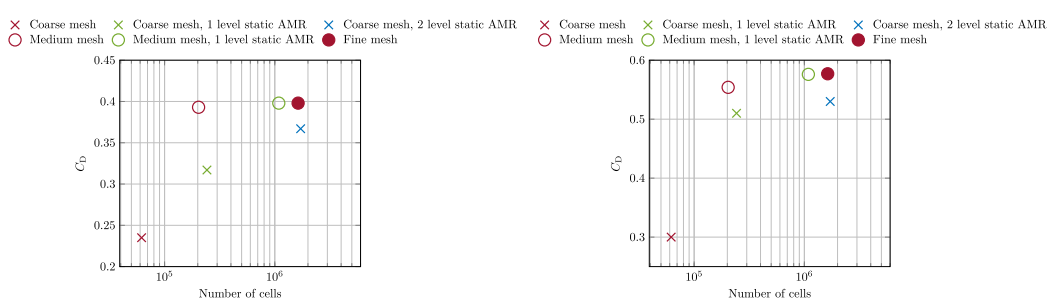

(a) Re = 300, Ma = 0.3, $\alpha = 0°$ **(b)** Re = 300, Ma = 2.0, $\alpha = 0°$

Fig. A.17. Convergence behaviour of the drag coefficient for a rod-like particle.

shapes as a function of the Mach number for all considered angles of attack. For angles of attack of 0° and 90°, the lift and torque coefficients are not shown, since they are zero for these flow configurations.

Appendix C. Summary of the full models to predict the drag, lift, and torque coefficients

In this appendix we give a summary of the full models for each non-spherical particle shape considered in this study. We exemplary choose the correlations for the incompressible limit of Zastawny et al. (2012), but any other correlation (e.g., Sanjeevi et al. (2018), Chéron et al. (2024)) for the respective particle shape and aspect ratio in the incompressible limit may be used. These full models can be directly employed in point particle simulations.

C.1. Drag coefficient

The proposed correlations for the drag coefficient of each studied particle shape are based on drag coefficient correlations in the incompressible flow regime and a compressible correction. Both are a

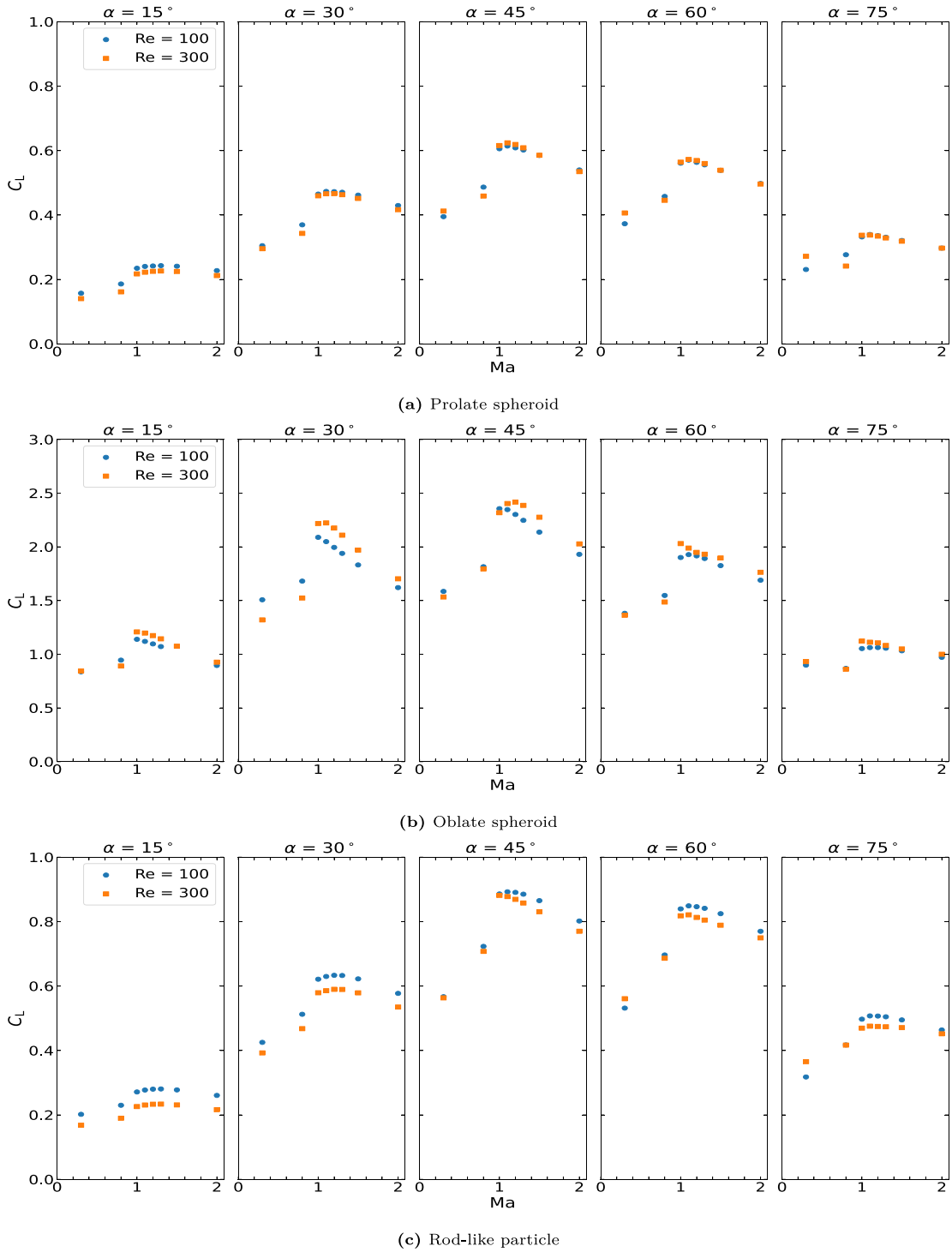

Fig. B.18. Variation of the lift coefficient C_L with Mach number Ma for different angles of attack considered for the three considered non-spherical particle shapes.

function of the particle Reynolds number, the Mach number, and the angle of attack. The general expression is defined as

$$C_D\left(\mathrm{Re_p}, \alpha, \mathrm{Ma}\right) = C_D\left(\mathrm{Re_p}, \alpha, \mathrm{Ma}=0\right)\left[1 + \mathcal{F}_D^{\mathrm{Ma}}\left(\mathrm{Re_p}, \alpha, \mathrm{Ma}\right)\right] \tag{C.1}$$

where C_D is the drag coefficient of a specific particle given as a function of the particle Reynolds number, angle of attack, and Mach number. This coefficient depends on the drag coefficient for equivalent particle Reynolds number and angle of attack in incompressible flow conditions, and an additional shape-dependent function, $\mathcal{F}_D^{\mathrm{Ma}}$ to account for the

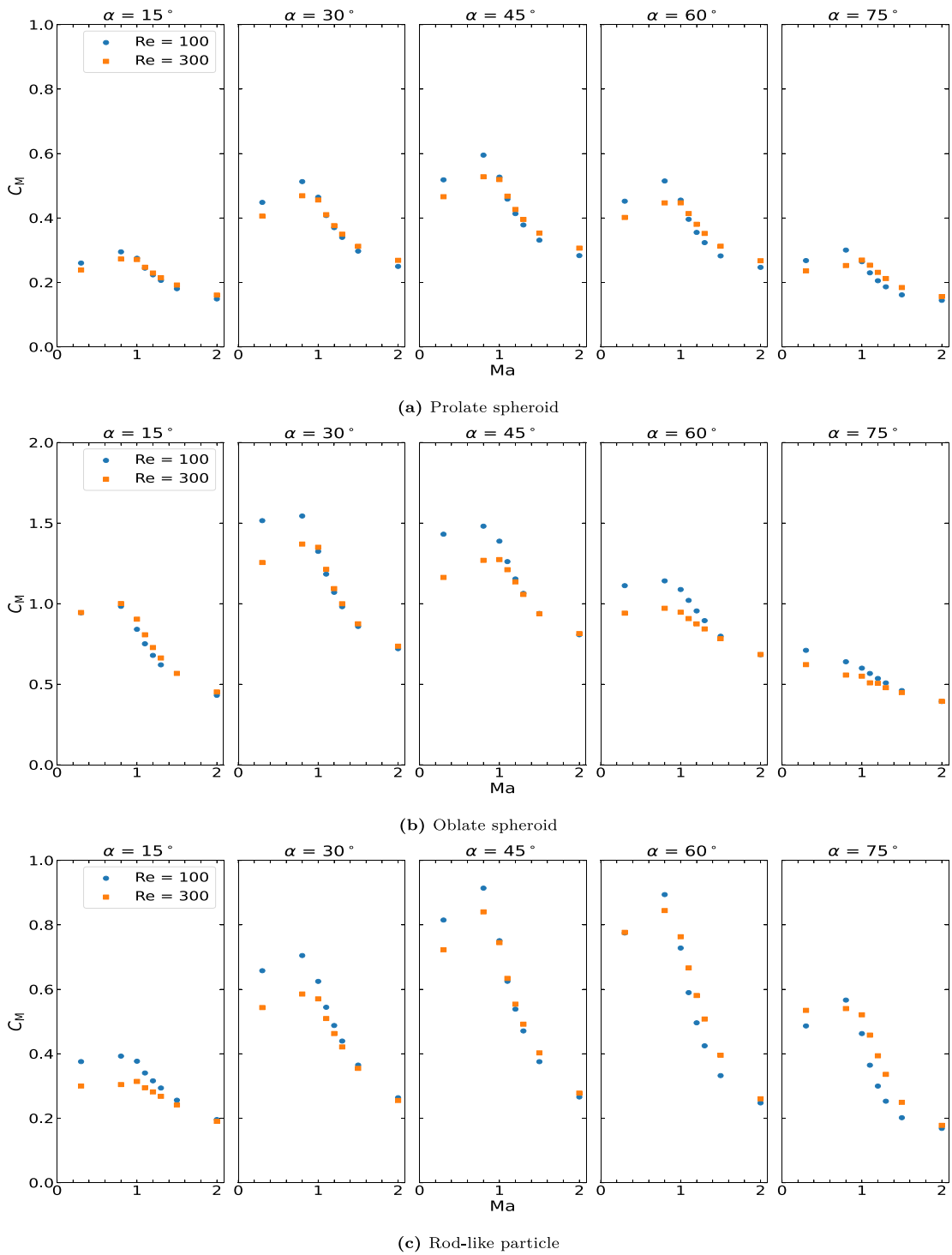

(a) Prolate spheroid

(b) Oblate spheroid

(c) Rod-like particle

Fig. B.19. Variation of the torque coefficient C_M with Mach number Ma for different angles of attack considered for the three considered non-spherical particle shapes.

Table C.4
List of the fitting coefficients in Eqs. (C.2), (C.3), and (C.4), used in the incompressible term based on the correlation of Zastawny et al. (2012).

Coefficient	Eq. (C.2)	Eq. (C.3)	Eq. (C.4)
a_0	2.0	1.96	2.12
a_1	5.1	5.82	20.35
a_2	0.48	0.44	0.98
a_3	15.52	15.56	2.77
a_4	1.05	1.068	0.396
a_5	24.68	35.41	29.14
a_6	0.98	0.96	0.97
a_7	3.19	3.63	3.66
a_8	0.21	0.05	0.16

change in the coefficient as a result of the compressibility of the flow.

The full model for the drag coefficient of the prolate spheroid, as the combination of the correlation of Zastawny et al. (2012) for the incompressible limit and ours for the compressible limit, is

$$C_D\left(\mathrm{Re_p},\alpha,\mathrm{Ma}\right)=\left[\left(\frac{a_1}{\mathrm{Re_p}^{a_2}}+\frac{a_3}{\mathrm{Re_p}^{a_4}}\right)+\left(\left(\frac{a_5}{\mathrm{Re_p}^{a_6}}+\frac{a_7}{\mathrm{Re_p}^{a_8}}\right)-\left(\frac{a_1}{\mathrm{Re_p}^{a_2}}+\frac{a_3}{\mathrm{Re_p}^{a_4}}\right)\right)\sin^{a_0}(\alpha)\right]\left[1+\frac{\left(\vartheta_1\mathrm{Re_p}+\vartheta_2\alpha^{\vartheta_3}\right)}{\left[1+\exp\left(-\vartheta_4(\mathrm{Ma}-\vartheta_5)\right)\right]}+\vartheta_6\exp\left(-\frac{(\mathrm{Ma}-\vartheta_7)^2}{\vartheta_8}\right)\right], \tag{C.2}$$

the full model for the oblate spheroid is

$$C_D\left(\mathrm{Re_p},\alpha,\mathrm{Ma}\right)=\left[\left(\frac{a_1}{\mathrm{Re_p}^{a_2}}+\frac{a_3}{\mathrm{Re_p}^{a_4}}\right)+\left(\left(\frac{a_5}{\mathrm{Re_p}^{a_6}}+\frac{a_7}{\mathrm{Re_p}^{a_8}}\right)-\left(\frac{a_1}{\mathrm{Re_p}^{a_2}}+\frac{a_3}{\mathrm{Re_p}^{a_4}}\right)\right)\sin^{a_0}(\alpha)\right]\left[1+\frac{\vartheta_1/\log(\mathrm{Re_p})\left(\vartheta_2\alpha/\pi\right)^{\vartheta_3(\mathrm{Re_p})^{\vartheta_4}}+\log(\mathrm{Re_p})/\vartheta_5-1}{\left[1+\exp\left(-\vartheta_6(\mathrm{Ma}-\vartheta_7)\right)\right]}+\vartheta_8\exp\left(-\frac{(\mathrm{Ma}-\vartheta_9)^2}{\vartheta_{10}}\right)\right], \tag{C.3}$$

and the full model for the rod-like particle is

$$C_D\left(\mathrm{Re_p},\alpha,\mathrm{Ma}\right)=\left[\left(\frac{a_1}{\mathrm{Re_p}^{a_2}}+\frac{a_3}{\mathrm{Re_p}^{a_4}}\right)+\left(\left(\frac{a_5}{\mathrm{Re_p}^{a_6}}+\frac{a_7}{\mathrm{Re_p}^{a_8}}\right)-\left(\frac{a_1}{\mathrm{Re_p}^{a_2}}+\frac{a_3}{\mathrm{Re_p}^{a_4}}\right)\right)\sin^{a_0}(\alpha)\right]\left[1+\frac{\vartheta_1\cdot\mathrm{Re_p}+\vartheta_2\cdot\left(\frac{\mathrm{Re_p}}{\vartheta_3}\right)^{\vartheta_4}\cdot\alpha^{\vartheta_5}}{\left[1.0+\exp\left(-\vartheta_6\cdot(\mathrm{Ma}-\vartheta_7)\right)\right]}+\left(\frac{\vartheta_8\cdot\alpha}{\mathrm{Re_p}}\right)^{\vartheta_9}\cdot\exp\left(-\frac{(\mathrm{Ma}-\vartheta_{10})^2}{\vartheta_{11}}\right)\right]. \tag{C.4}$$

The fitting coefficients a_i and ϑ_i for the drag coefficients of all three considered particle shapes are given in Tables C.4 and C.5.

C.2. Lift coefficient

Following a similar approach as for the drag coefficients, the proposed correlation for the lift coefficient of each studied particle shape is based on the lift coefficient in the incompressible flow regime from Zastawny et al. (2012) and a compressible correction that is a function of the particle Reynolds number, the Mach number, and the angle of attack. The general expression is defined as

$$C_L\left(\mathrm{Re_p},\alpha,\mathrm{Ma}\right)=C_L\left(\mathrm{Re_p},\alpha,\mathrm{Ma}=0\right)+\mathcal{F}_L^{\mathrm{Ma}}\left(\mathrm{Re_p},\alpha,\mathrm{Ma}\right) \tag{C.5}$$

where C_L is the lift coefficient of a specific particle given as a function of the particle Reynolds number, angle of attack, and Mach number. This coefficient is obtained from the summation of the lift coefficient for equivalent particle Reynolds number and angle of attack in incompressible flow conditions, and an additional shape-dependent function, $\mathcal{F}_L^{\mathrm{Ma}}$, to account for the change in the lift coefficient in case of compressible flow. The full model for the lift coefficient of the prolate spheroid is

$$C_L\left(\mathrm{Re_p},\alpha,\mathrm{Ma}\right)=\left[\left(\frac{b_1}{\mathrm{Re_p}^{b_2}}+\frac{b_3}{\mathrm{Re_p}^{b_4}}\right)\sin(\alpha)^{b_5+b_6\mathrm{Re_p}^{b_7}}\cos(\alpha)^{b_8+b_9\mathrm{Re_p}^{b_{10}}}\right]+\frac{\vartheta_1\log\left(\mathrm{Re_p}\right)^{\vartheta_2}}{\left[1+\exp\left(\vartheta_3(\mathrm{Ma}-\vartheta_4)\right)\right]}\cos\left(\Psi_1\left(\alpha,\mathrm{Re_p}\right)\right)\sin\left(\Psi_1\left(\alpha,\mathrm{Re_p}\right)\right)+\vartheta_5\exp\left(\frac{-(\mathrm{Ma}-\vartheta_6)^2}{\vartheta_7}\right)\left[\cos\left(\Psi_2\left(\alpha,\mathrm{Re_p}\right)\right)\sin\left(\Psi_2\left(\alpha,\mathrm{Re_p}\right)\right)\right]^{\vartheta_8}, \tag{C.6}$$

with

$$\Psi_1=\frac{\pi}{2}\left(\alpha\frac{2}{\pi}\right)^{1+4.185\times10^{-5}\log\left(\mathrm{Re_p}\right)^{-10.5}} \tag{C.7}$$

and

$$\Psi_2=\frac{\pi}{2}\left(\alpha\frac{2}{\pi}\right)^{1+2.146\log\left(\mathrm{Re_p}\right)^{-1.444}}. \tag{C.8}$$

The full model for the oblate spheroid is

$$C_L\left(\mathrm{Re_p},\alpha,\mathrm{Ma}\right)=\left[\left(\frac{b_1}{\mathrm{Re_p}^{b_2}}+\frac{b_3}{\mathrm{Re_p}^{b_4}}\right)\sin(\alpha)^{b_5+b_6\mathrm{Re_p}^{b_7}}\cos(\alpha)^{b_8+b_9\mathrm{Re_p}^{b_{10}}}\right]+\frac{\vartheta_1\log(\mathrm{Re_p})}{\left[1+\exp\left(-\vartheta_2(\mathrm{Ma}-\vartheta_3)\right)\right]}\cos(\alpha)^{\vartheta_4}\sin(\alpha)^{\vartheta_5}+\vartheta_6\exp\left(-\frac{(\mathrm{Ma}-\vartheta_7)^2}{\vartheta_8}\right)\cos(\alpha)\sin(\alpha), \tag{C.9}$$

and the full model for the rod-like particle is

$$C_L\left(\mathrm{Re_p},\alpha,\mathrm{Ma}\right)=\left[\left(\frac{b_1}{\mathrm{Re_p}^{b_2}}+\frac{b_3}{\mathrm{Re_p}^{b_4}}\right)\sin(\alpha)^{b_5+b_6\mathrm{Re_p}^{b_7}}\cos(\alpha)^{b_8+b_9\mathrm{Re_p}^{b_{10}}}\right]+\frac{\left(\vartheta_1/\log\left(\mathrm{Re_p}\right)\right)^{\vartheta_2}}{\left[1+\exp\left(\vartheta_3\cdot(\mathrm{Ma}-\vartheta_4)\right)\right]}\cos\left(\Psi_1\left(\alpha,\mathrm{Re_p}\right)\right)\sin\left(\Psi_1\left(\alpha,\mathrm{Re_p}\right)\right)+\vartheta_5\exp\left(\frac{-(\mathrm{Ma}-\vartheta_6)^2}{\vartheta_7}\right)\left[\cos\left(\Psi_2\left(\alpha,\mathrm{Re_p}\right)\right)\sin\left(\Psi_2\left(\alpha,\mathrm{Re_p}\right)\right)\right]^{\vartheta_8}, \tag{C.10}$$

with

$$\Psi_1=\frac{\pi}{2}\left(\alpha\frac{2}{\pi}\right)^{1+2.471\log\left(\mathrm{Re_p}\right)^{-1.50}} \tag{C.11}$$

and

$$\Psi_2=\frac{\pi}{2}\left(\alpha\frac{2}{\pi}\right)^{1+1630.79\left(1/\log\left(\mathrm{Re_p}\right)\right)^{6.00}}. \tag{C.12}$$

Table C.5
List of the fitting coefficients in Eqs. (C.2), (C.3), and (C.4), used in the correlation to predict the change in the drag coefficient in the case of compressible flow.

	ϑ_1	ϑ_2	ϑ_3	ϑ_4	ϑ_5	ϑ_6	ϑ_7	ϑ_8	ϑ_9	ϑ_{10}	ϑ_{11}
Eq. (C.2)	1.55×10^{-3}	0.201	0.492	15.6	0.878	0.183	1.21	0.142	–	–	–
Eq. (C.3)	6.07	0.269	4.40×10^{-5}	2.10	3.90	21.3	0.853	0.130	1.17	0.252	–
Eq. (C.4)	1.14×10^{-3}	0.121	2.64	0.0983	1.40	14.6	0.861	3.94	0.631	1.20	0.330

Table C.6
List of fitting coefficients in Eqs. (C.6), (C.9), and (C.10), used in the correlation to predict the change in the lift coefficient in the incompressible limit.

Coefficient	Eq. (C.6)	Eq. (C.9)	Eq. (C.10)
b_1	6.079	12.111	8.652
b_2	0.898	1.036	0.815
b_3	0.704	3.887	0.407
b_4	−0.028	0.109	−0.197
b_5	1.067	0.812	0.978
b_6	0.0025	0.249	0.036
b_7	0.818	−0.198	0.451
b_8	1.049	5.821	1.359
b_9	0.0	4.717	−0.43
b_{10}	0.0	0.007	0.007

Table C.7
List of the fitting coefficients in Eqs. (C.6), (C.9), and (C.10), used in the correlation to predict the change in the lift coefficient in case of compressible flow.

	ϑ_1	ϑ_2	ϑ_3	ϑ_4	ϑ_5	ϑ_6	ϑ_7	ϑ_8
Eq. (C.6)	1.17	−0.735	−21.8	0.870	0.277	1.12	0.217	2.00
Eq. (C.9)	0.535	130	0.807	1.84	1.56	−0.996	2.25	0.516
Eq. (C.10)	2.43	1.20	−24.8	0.807	2.43	1.24	0.237	4.22

Table C.8
List of fitting coefficients in Eqs. (C.14), used in the correlation to predict the change in the torque coefficient in the incompressible limit.

Coefficient	Prolate spheroid	Oblate spheroid	Rod-like
c_1	2.078	3.782	0.011
c_2	0.279	0.237	−0.656
c_3	0.372	2.351	8.909
c_4	0.018	0.236	0.396
c_5	0.98	−0.394	2.926
c_6	0.0	1.615	−1.28
c_7	0.0	−0.044	0.037
c_8	1.0	−0.537	−15.236
c_9	0.0	1.805	16.757
c_{10}	0.0	−0.037	−0.006

The fitting coefficients b_i and ϑ_i for the lift coefficients of all three considered particle shapes are given in Tables C.6 and C.7.

C.3. Torque coefficient

As for the drag and lift coefficients, the proposed correlation for the torque coefficient of each studied particle shape is based on the torque coefficient in the incompressible flow regime (here exemplary Zastawny et al. (2012)) and a compressible correction that is a function of the particle Reynolds number, the Mach number, and the angle of attack. The general expression is defined as

$$C_{\mathrm{M}}\left(\mathrm{Re_p}, \alpha, \mathrm{Ma}\right) = C_{\mathrm{M}}\left(\mathrm{Re_p}, \alpha, \mathrm{Ma}=0\right) + \mathcal{F}_{\mathrm{M}}^{\mathrm{Ma}}\left(\mathrm{Re_p}, \alpha, \mathrm{Ma}\right) \tag{C.13}$$

where C_{M} is the torque coefficient of a specific particle given as a function of the particle Reynolds number, the Mach number, and the angle of attack. This coefficient is obtained from the summation of the torque coefficient for equivalent particle Reynolds number and angle of attack in incompressible flow conditions, and an additional shape-dependent function, $\mathcal{F}_{\mathrm{M}}^{\mathrm{Ma}}$, to account for the change in the torque coefficient in case of compressible flow. The full model for the torque coefficient of all three considered particle shapes is

$$\begin{aligned} C_{\mathrm{M}}\left(\mathrm{Re_p}, \alpha, \mathrm{Ma}\right) = & \left[\left(\frac{c_1}{\mathrm{Re_p}^{c_2}} + \frac{c_3}{\mathrm{Re_p}^{c_4}}\right) \sin\left(\alpha\right)^{c_5 + c_6 \mathrm{Re_p}^{c_7}} \cos\left(\alpha\right)^{c_8 + c_9 \mathrm{Re_p}^{c_{10}}}\right] \\ & + \frac{\vartheta_1 \mathrm{Re_p} + \vartheta_2 \left(\mathrm{Re_p}/\vartheta_3\right)^{\vartheta_4}}{1 + \exp\left(-\vartheta_5\left(\mathrm{Ma} - \vartheta_6\right)\right)} \cdot \left(\cos\left(\Psi_1\right) \sin\left(\Psi_1\right)\right)^{\vartheta_7} \\ & + \left(\frac{\vartheta_8 \alpha}{\vartheta_{10}}\right)^{\vartheta_9} \cdot \left(\frac{\vartheta_{11} \mathrm{Re_p}}{\vartheta_{13}}\right)^{\vartheta_{12}} \cdot \exp\left(\frac{-\left(\mathrm{Ma} - \vartheta_{14}\right)^2}{\vartheta_{15}}\right) \\ & \cdot \left(\cos\left(\Psi_2\right) \sin\left(\Psi_2\right)\right)^{\vartheta_{16}}, \end{aligned} \tag{C.14}$$

with

$$\Psi_1 = \frac{\pi}{2}\left(\alpha \frac{2}{\pi}\right)^{\vartheta_{17}} \tag{C.15}$$

and

$$\Psi_2 = \frac{\pi}{2}\left(\alpha \frac{2}{\pi}\right)^{\vartheta_{18}}. \tag{C.16}$$

Table C.9
List of the fitting coefficients in Eq. (C.14), used in the correlation to predict the change in the torque coefficient in case of compressible flow.

	Prolate	Oblate	Rod-like
ϑ_1	2.28×10^{-4}	-4.43×10^{-3}	-2.32×10^{-5}
ϑ_2	−0.444	−0.759	−1.15
ϑ_3	157	203	127
ϑ_4	−0.223	−1.03	−0.134
ϑ_5	15.1	5.93	12.3
ϑ_6	1.01	1.22	1.03
ϑ_7	0.993	1.11	1.04
ϑ_8	4.96×10^{-2}	3.18×10^{-9}	13.8
ϑ_9	1.44	8.95×10^{-2}	1.88
ϑ_{10}	7.42×10^{-3}	3.59×10^{-2}	3.64
ϑ_{11}	3.81×10^{-2}	3.89	0.520
ϑ_{12}	1.68×10^{-2}	0.569	0.158
ϑ_{13}	5.86×10^{-9}	10.8	1.22×10^{-6}
ϑ_{14}	1.10	1.98	1.18
ϑ_{15}	9.29×10^{-3}	1.04	3.71×10^{-3}
ϑ_{16}	1.05	2.50	1.16
ϑ_{17}	0.164	1.17	0.157
ϑ_{18}	1.04	0.809	1.32

The fitting coefficients c_i and ϑ_i for the torque coefficients of all three considered particle shapes are given in Tables C.8 and C.9.

Data availability

The data that support the findings of this study are reproducible and files to regenerate the data as well as an executable to implement the correlations to predict the drag, lift, and torque coefficients are openly available in the repository with DOI 10.5281/zenodo.14283844.

References

Anderson, J.D., 2003. Modern Compressible Flow: with a Historical Perspective. McGraw-Hill New York.

Bashforth, F., 1870. Reports on Experiments Made with the Bashforth Chronograph To Determine the Resistance of the Air To the Motion of Projectiles. H.M. Stationery Office, Google-Books-ID: cqZYAAAAcAAJ.

Bhagat, A.M., Goswami, P.S., 2022. Effect of rough wall on drag, lift, and torque on an ellipsoidal particle in a linear shear flow. Phys. Fluids 34, 083312. http://dx.doi.org/10.1063/5.0093232.

Capecelatro, J., 2022. Modeling high-speed gas–particle flows relevant to spacecraft landings. Int. J. Multiph. Flow 150, 104008. http://dx.doi.org/10.1016/j.ijmultiphaseflow.2022.104008, URL https://www.sciencedirect.com/science/article/pii/S0301932222000301.

Capecelatro, J., Longest, W., Boerman, C., Sulaiman, M., Sundaresan, S., 2022. Recent developments in the computational simulation of dry powder inhalers. Adv. Drug Deliv. Rev. 114461. http://dx.doi.org/10.1016/j.addr.2022.114461, URL https://www.sciencedirect.com/science/article/pii/S0169409X22003519.

Capecelatro, J., Wagner, J.L., 2024. Gas–particle dynamics in high-speed flows. Annu. Rev. Fluid Mech. 56, 379–403. http://dx.doi.org/10.1146/annurev-fluid-121021-015818, URL https://www.annualreviews.org/doi/10.1146/annurev-fluid-121021-015818.

Carlson, D.J., Hoglund, R.F., 1964. Particle drag and heat transfer in rocket nozzles. AIAA J. 2, 1980–1984. http://dx.doi.org/10.2514/3.2714, URL https://arc.aiaa.org/doi/10.2514/3.2714.

Chéron, V., Evrard, F., van Wachem, B., 2024. Drag, lift and torque correlations for axi-symmetric rod-like non-spherical particles in locally linear shear flows. Int. J. Multiphase Flow 171, 104692. http://dx.doi.org/10.1016/j.ijmultiphaseflow.2023.104692, URL https://www.sciencedirect.com/science/article/pii/S0301932223003129.

Chéron, V., van Wachem, B., 2024. Drag, lift, and torque correlations for axi-symmetric rod-like non-spherical particles in linear wall-bounded shear flow. Int. J. Multiph. Flow 104906. http://dx.doi.org/10.1016/j.ijmultiphaseflow.2024.104906, URL https://linkinghub.elsevier.com/retrieve/pii/S0301932224001836.

Clift, R., Gauvin, W.H., 1971. Motion of entrained particles in gas streams. Can. J. Chem. Eng. 49, 439–448. http://dx.doi.org/10.1002/cjce.5450490403, URL http://doi.wiley.com/10.1002/cjce.5450490403.

Dabade, V., Marath, N.K., Subramanian, G., 2016. The effect of inertia on the orientation dynamics of anisotropic particles in simple shear flow. J. Fluid Mech. 791, 631–703. http://dx.doi.org/10.1017/jfm.2016.14, URL https://www.cambridge.org/core/journals/journal-of-fluid-mechanics/article/abs/effect-of-inertia-on-the-orientation-dynamics-of-anisotropic-particles-in-simple-shear-flow/946CB5A981ABAADF546483CCFE7AD0C8.

Denner, F., Evrard, F., van Wachem, B., 2020. Conservative finite-volume framework and pressure-based algorithm for flows of incompressible, ideal-gas and real-gas fluids at all speeds. J. Comput. Phys. 409, 109348. http://dx.doi.org/10.1016/j.jcp.2020.109348, URL https://linkinghub.elsevier.com/retrieve/pii/S0021999120301224.

Fillingham, P., Vaddi, R.S., Bruning, A., Israel, G., Novosselov, I.V., 2021. Drag, lift, and torque on a prolate spheroid resting on a smooth surface in a linear shear flow. Powder Technol. 377, 958–965. http://dx.doi.org/10.1016/j.powtec.2020.09.042, URL https://www.sciencedirect.com/science/article/pii/S0032591020309062.

Fröhlich, K., Meinke, M., Schröder, W., 2020. Correlations for inclined prolates based on highly resolved simulations. J. Fluid Mech. 901 (A5), http://dx.doi.org/10.1017/jfm.2020.482, URL https://www.cambridge.org/core/product/identifier/S0022112020004826/type/journal_article.

Happel, J., Brenner, H., 1981. Low Reynolds number hydrodynamics. In: Mechanics of fluids and transport processes, vol. 1, Springer Netherlands, Dordrecht, http://dx.doi.org/10.1007/978-94-009-8352-6, URL http://link.springer.com/10.1007/978-94-009-8352-6.

Henderson, C.B., 1976. Drag coefficients of spheres in continuum and rarefied flows. AIAA J. 14, 707–708. http://dx.doi.org/10.2514/3.61409, URL https://arc.aiaa.org/doi/10.2514/3.61409.

Hogan, N.C., Taberner, A.J., Jones, L.A., Hunter, I.W., 2015. Needle-free delivery of macromolecules through the skin using controllable jet injectors. Expert Opin. Drug Delivery 12, 1637–1648. http://dx.doi.org/10.1517/17425247.2015.1049531, URL http://www.t{andf}online.com/doi/full/10.1517/17425247.2015.1049531.

Hölzer, A., Sommerfeld, M., 2008. New simple correlation formula for the drag coefficient of non-spherical particles. Powder Technol. 184, 361–365. http://dx.doi.org/10.1016/j.powtec.2007.08.021, URL http://linkinghub.elsevier.com/retrieve/pii/S0032591007004792.

Jacobs, E.N., 1929. Sphere drag tests in the variable density wind tunnel. URL https://digital.library.unt.edu/ark:/67531/metadc54020/. number: NACA-TN-312.

Johansson, R., 2019. Numerical Python: Scientific Computing and Data Science Applications with Numpy, SciPy and Matplotlib. A Press, Berkeley, CA, http://dx.doi.org/10.1007/978-1-4842-4246-9, URL http://link.springer.com/10.1007/978-1-4842-4246-9.

Kaskas, A., 1964. Berechnung der stationären und instationären Bewegung von Kugeln in ruhenden und strömenden Medien (Master's thesis). Lehrstuhl fuer Thermodynamik und Verfahrenstechnik der T. U. Berlin. Germany., URL https://cir.nii.ac.jp/crid/1572824500138829056.

Loth, E., 2008. Lift of a solid spherical particle subject to vorticity and/or spin. AIAA J. 46, 801–809. http://dx.doi.org/10.2514/1.29159.

Loth, E., Tyler Daspit, J., Jeong, M., Nagata, T., Nonomura, T., 2021. Supersonic and hypersonic drag coefficients for a sphere. AIAA J. 3261–3274. http://dx.doi.org/10.2514/1.J060153, URL https://arc.aiaa.org/doi/10.2514/1.J060153.

Mando, M., Rosendahl, L., 2010. On the motion of non-spherical particles at high Reynolds number. Powder Technol. 202, 1–13. http://dx.doi.org/10.1016/j.powtec.2010.05.001, URL http://www.sciencedirect.com/science/article/pii/S0032591010002391.

Michaelides, E.E., Sommerfeld, S., van Wachem, B., 2022. Multiphase Flows with Droplets and Particles, third ed. CRC Press, Boca Raton, http://dx.doi.org/10.1201/9781003089278.

Nagata, T., Noguchi, A., Nonomura, T., Ohtani, K., Asai, K., 2020a. Experimental investigation of transonic and supersonic flow over a sphere for Reynolds numbers of 103–105 by free-flight tests with schlieren visualization. Shock Waves 30, 139–151. http://dx.doi.org/10.1007/s00193-019-00924-0.

Nagata, T., Nonomura, T., Takahashi, S., Fukuda, K., 2020b. Direct numerical simulation of subsonic, transonic and supersonic flow over an isolated sphere up to a Reynolds number of 1000. J. Fluid Mech. 904, A36. http://dx.doi.org/10.1017/jfm.2020.629, URL https://www.cambridge.org/core/journals/journal-of-fluid-mechanics/article/direct-numerical-simulation-of-subsonic-transonic-and-supersonic-flow-over-an-isolated-sphere-up-to-a-reynolds-number-of-1000/24251E57F95CBFC00737F3EB3BB396BA, publisher: Cambridge University Press.

Nagata, T., Nonomura, T., Takahashi, S., Mizuno, Y., Fukuda, K., 2016. Investigation on subsonic to supersonic flow around a sphere at low Reynolds number of between 50 and 300 by direct numerical simulation. Phys. Fluids 28, 056101. http://dx.doi.org/10.1063/1.4947244, URL http://aip.scitation.org/doi/10.1063/1.4947244.

Nagata, T., Nonomura, T., Takahashi, S., Mizuno, Y., Fukuda, K., 2018. Direct numerical simulation of flow past a transversely rotating sphere up to a Reynolds number of 300 in compressible flow. J. Fluid Mech. 857, 878–906. http://dx.doi.org/10.1017/jfm.2018.756.

Ouchene, R., 2020. Numerical simulation and modeling of the hydrodynamic forces and torque acting on individual oblate spheroids. Phys. Fluids 32, 073303. http://dx.doi.org/10.1063/5.0011618, URL https://pubs.aip.org/aip/pof/article/1060398.

Ouchene, R., Khalij, M., Arcen, B., Tanière, A., 2016. A new set of correlations of drag, lift and torque coefficients for non-spherical particles and large Reynolds numbers. Powder Technol. 303, 33–43. http://dx.doi.org/10.1016/j.powtec.2016.07.067, URL http://linkinghub.elsevier.com/retrieve/pii/S0032591016304594.

Ouchene, R., Khalij, M., Tanière, A., Arcen, B., 2015. Drag, lift and torque coefficients for ellipsoidal particles: From low to moderate particle Reynolds numbers. Comput. & Fluids 113, 53–64. http://dx.doi.org/10.1016/j.compfluid.2014.12.005, URL http://linkinghub.elsevier.com/retrieve/pii/S004579301400468X.

Parmar, M., Haselbacher, A., Balachandar, S., 2010. Improved drag correlation for spheres and application to shock-tube experiments. AIAA J. 48, 1273–1276. http://dx.doi.org/10.2514/1.J050161, URL https://arc.aiaa.org/doi/10.2514/1.J050161.

Roos, F.W., Willmarth, W.W., 1971. Some experimental results on sphere and disk drag. AIAA J. 9, 285–291. http://dx.doi.org/10.2514/3.6164, URL https://arc.aiaa.org/doi/10.2514/3.6164.

Rosendahl, L., 2000. Using a multi-parameter particle shape description to predict the motion of non-spherical particle shapes in swirling flow. Appl. Math. Model. 24, 11–25. http://dx.doi.org/10.1016/S0307-904X(99)00023-2, URL http://linkinghub.elsevier.com/retrieve/pii/S0307904X99000232.

Salman, A.D., Verba, A., 1988. New aproximate equations to estimate the drag coefficient of different particles of regular shape. Periodica Polytech. Chem. Eng. 32, 261–276, URL https://pp.bme.hu/ch/article/view/2794. number: 4.

Sanjeevi, S.K.P., Dietiker, J.F., Padding, J.T., 2022. Accurate hydrodynamic force and torque correlations for prolate spheroids from Stokes regime to high Reynolds numbers. Chem. Eng. J. 444, 136325. http://dx.doi.org/10.1016/j.cej.2022.136325, URL https://www.sciencedirect.com/science/article/pii/S1385894722018204.

Sanjeevi, S.K.P., Kuipers, J.A.M., Padding, J.T., 2018. Drag, lift and torque correlations for non-spherical particles from Stokes limit to high Reynolds numbers. Int. J. Multiph. Flow 106, 325–337. http://dx.doi.org/10.1016/j.ijmultiphaseflow.2018.05.011, URL http://www.sciencedirect.com/science/article/pii/S0301932217307851.

Short, B.J., 1967. Dynamic Flight Behavior of a Ballasted Sphere At Mach Numbers from 0.4 To 14.5. Technical Report NASA-TN-D-4198, NASA Ames Research Center, nTRS Author Affiliations: NASA Ames Research Center NTRS Document ID: 19670029052 NTRS Research Center: Legacy CDMS (CDMS).

Singh, N., Kroells, M., Li, C., Ching, E., Ihme, M., Hogan, C.J., Schwartzentruber, T.E., 2022. General drag coefficient for flow over spherical particles. AIAA J. 60, 587–597. http://dx.doi.org/10.2514/1.J060648, publisher: American Institute of Aeronautics and Astronautics _eprint.

Spearman, M.L., Braswell, D.O., 1993. Aerodynamics of a sphere and an oblate spheroid for Mach numbers from 0.6 to 10.5 including some effects of test conditions. Technical Report NAS 1.15:109016.

Stokes, G.G., 1851. On the effect of the internal friction of fluids on the motion of pendulums. Trans. Cambridge Philos. Soc. 9 (8).

Tenneti, S., Garg, R., Subramaniam, S., 2011. Drag law for monodisperse gas–solid systems using particle-resolved direct numerical simulation of flow past fixed assemblies of spheres. Int. J. Multiph. Flow 37, 1072–1092. http://dx.doi.org/10.1016/j.ijmultiphaseflow.2011.05.010, URL http://www.sciencedirect.com/science/article/pii/S0301932211001170.

Theofanous, T.G., Mitkin, V., Chang, C.H., 2018. Shock dispersal of dilute particle clouds. J. Fluid Mech. 841, 732–745. http://dx.doi.org/10.1017/jfm.2018.110, URL https://www.cambridge.org/core/journals/journal-of-fluid-mechanics/article/shock-dispersal-of-dilute-particle-clouds/FBE48DECAA77FE8A0DF13883837D9FB3, publisher: Cambridge University Press.

van Wachem, B., Zastawny, M., Zhao, F., Mallouppas, G., 2015. Modelling of gas–solid turbulent channel flow with non-spherical particles with large Stokes numbers. Int. J. Multiph. Flow 68, 80–92. http://dx.doi.org/10.1016/j.ijmultiphaseflow.2014.10.006, URL http://linkinghub.elsevier.com/retrieve/pii/S0301932214001931.

Villafuerte, J. (Ed.), 2015. Modern Cold Spray. Springer International Publishing, Cham, http://dx.doi.org/10.1007/978-3-319-16772-5, URL http://link.springer.com/10.1007/978-3-319-16772-5.

Wadell, H., 1934. The coefficient of resistance as a function of Reynolds number for solids of various shapes. J. Franklin Inst. April, 459–490, URL http://www.sciencedirect.com/science/article/pii/S0016003234905081.

Xiao, C.N., Denner, F., van Wachem, B., 2017. Fully-coupled pressure-based finite-volume framework for the simulation of fluid flows at all speeds in complex geometries. J. Comput. Phys. 346, 91–130. http://dx.doi.org/10.1016/j.jcp.2017.06.009, URL http://linkinghub.elsevier.com/retrieve/pii/S0021999117304540.

Zastawny, M., Mallouppas, G., Zhao, F., van Wachem, B., 2012. Modelling of gas-solid turbulent flows with non-spherical particles. In: 8th International Conference on Multiphase Flow. ICMF 2013, Elsevier Ltd., pp. 227–239. http://dx.doi.org/10.1016/j.ijmultiphaseflow.2011.09.004, URL http://linkinghub.elsevier.com/retrieve/pii/S0301932211002047.